

**SINGLE LINK FLEXIBLE
BEAM TESTBED PROJECT**

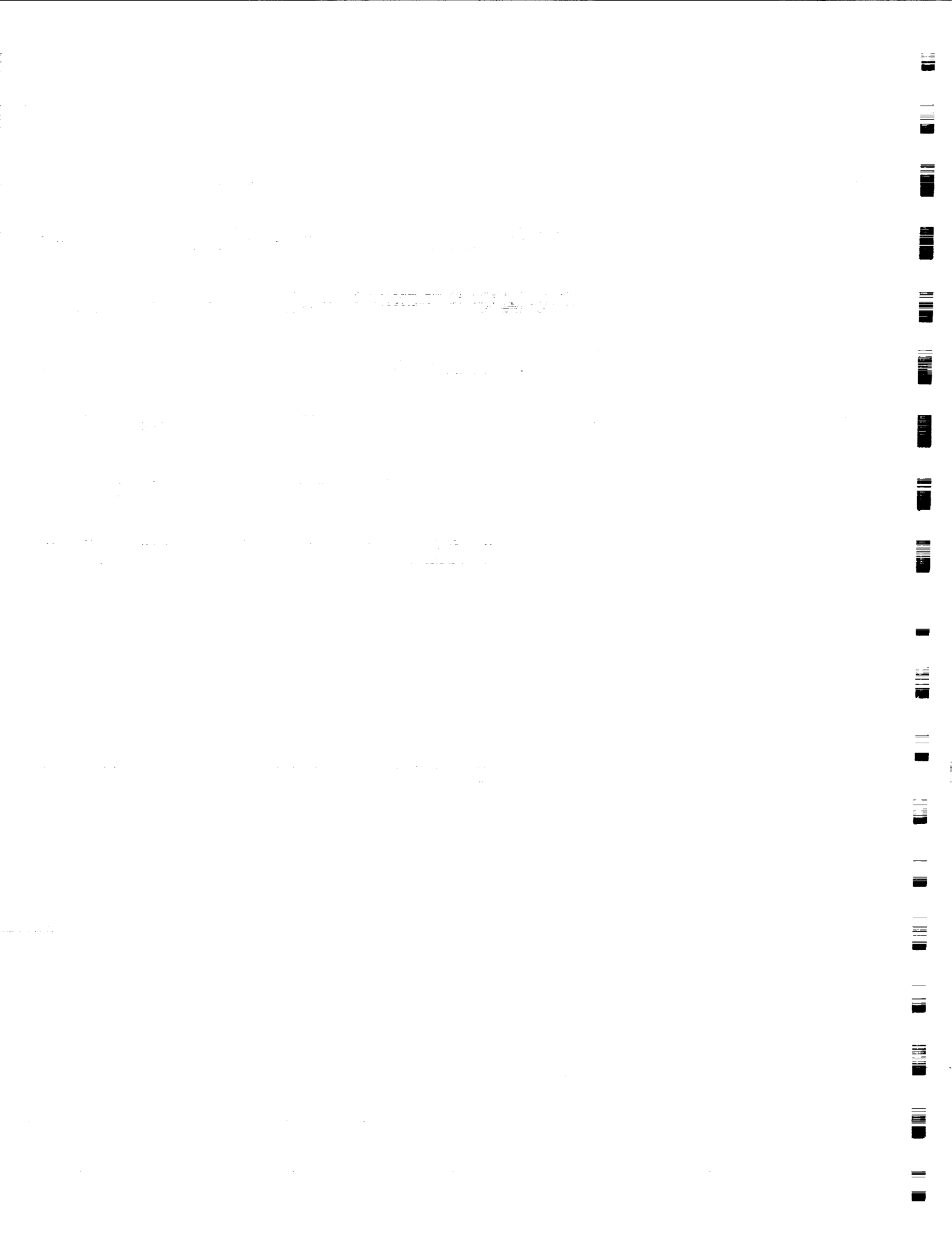
by

Declan Hughes

Rensselaer Polytechnic Institute
Electrical, Computer, and Systems Engineering Department
Troy, New York 12180-3590

July 1992

CIRSSE REPORT #120



CONTENTS

LIST OF TABLES	v
LIST OF FIGURES	vi
ACKNOWLEDGMENTS	viii
ABSTRACT	ix
INTRODUCTION	x
1. Hardware	1
1.1 Overview	1
1.2 Selecting the Flexible Beam	1
1.3 Actuator	3
1.4 Sensors	5
1.4.1 Hub Angle	5
1.4.2 Beam Strain	6
1.5 Computer	6
1.5.1 Real Time Computer	6
1.5.2 Development Host Computer	8
1.5.3 Computer to Signal Interface	8
2. Software	10
2.1 Software Overview	10
2.2 Program Description	12
2.3 Resetting Signal Offsets	13
3. Beam Modeling	15
3.1 Beam Analytical Modeling	15
3.1.1 Linear Differential Equations	15
3.1.2 Normal Mode Form	16
3.1.3 Finite State Space Normal Mode Approximation	20
3.2 Hub Actuator	20
3.3 Hub Angle Sensor	21

1. The first part of the document discusses the importance of maintaining accurate records of all transactions.

2. It is essential to ensure that all entries are supported by appropriate documentation and receipts.

3. Regular audits should be conducted to verify the accuracy of the records and identify any discrepancies.

4. The second part of the document outlines the procedures for handling disputes and resolving conflicts.

5. It is important to establish clear communication channels and protocols for addressing any issues that arise.

6. The document also provides guidance on how to maintain confidentiality and protect sensitive information.

7. Finally, it emphasizes the need for ongoing training and education to ensure that all staff members are up-to-date on the latest practices and regulations.

8. The third part of the document discusses the role of technology in streamlining operations and improving efficiency.

9. It highlights the benefits of using specialized software and tools to manage data and automate repetitive tasks.

10. The document also addresses the importance of data security and implementing robust cybersecurity measures.

11. In conclusion, this document provides a comprehensive overview of the key principles and practices for effective record-keeping and dispute resolution.

12. It is hoped that these guidelines will help organizations to maintain high standards of accuracy and integrity in their operations.

3.3.1	Angle to Voltage Conversion	22
3.4	Beam Strain Sensors	22
3.4.1	Strain Gage Geometry	23
3.4.2	Curvature-Strain Linear Relationship	26
3.4.3	Curvature-Strain Non-linear Relationship	27
3.4.4	Strain to Voltage Conversion	28
3.4.5	Strain Gage Signal Conditioner	28
3.5	Computer Input and Output	29
3.6	Complete Testbed State Space Model	30
3.7	Model Structural Features	31
3.8	Model Identification	33
3.8.1	Oscillation Frequencies	34
3.8.2	Damping coefficients	34
3.8.3	Modal Gains	35
3.8.4	Identification Improvements	35
4.	Control Design	37
4.1	Overview	37
4.2	Positive Realness	39
4.3	The Passivity Theorem	41
4.4	Hub Angle PD Compensator	42
4.4.1	Closed Loop Stability	42
4.4.2	Rigid Body Mode Plant	43
4.4.3	Root Locus Design	44
4.5	Synthesized Positive Real Output Controller (static feedback)	48
4.5.1	Selecting C_{sprd} (decoupled version)	51
4.5.2	Selecting C_{spr} (coupled version)	52
4.6	State Estimation	52
4.6.1	Full State Observers with Uncompensated Modes Effects	54
4.6.2	Reduced Order (Luenberger) Observer with Uncompensated Modes Effects	56
5.	Simulation and Experimental Results	58
5.1	Simulation Results with Ideal Observer	58

5.2 Closed Loop Observers Effects	61
5.3 Experimental Results with Reduced Order Luenberger Observer . . .	63
CONCLUSIONS	68
LITERATURE CITED	69
APPENDICES	70
A. Beam and Actuator Physical Parameters	70

LIST OF TABLES

Table 1.1	Candidate Beam Materials	3
Table 3.1	Beam Normal Mode Parameters	19
Table 4.1	PD Compensator Gains	46
Table 4.2	Compensator Pole Parameters	47
Table 4.3	Lyapunov Equation relative Weights	51
Table A.1	Aluminum Beam Material Parameters	70
Table A.2	Beam Derived Parameters	70
Table A.3	Motor Parameters	71
Table A.4	Hub Derived Parameters	71

LIST OF FIGURES

Figure 1.1	Testbed Physical System	2
Figure 2.1	Software Flow Diagram #1 (High level)	11
Figure 2.2	Software Flow Diagram #1 (High level)	12
Figure 3.1	Beam Model Coordinate Frames	16
Figure 3.2	Testbed Physical System	17
Figure 3.3	First Four Normal Mode Shapes	18
Figure 3.4	Beam and Strain Gage Cross Section	24
Figure 3.5	Beam Curvature Geometry	24
Figure 3.6	Strain Gage Wheatstone Bridge	29
Figure 3.7	Finite Linear Model Bode Plots	32
Figure 3.8	Normal Mode Linear Model Structure	33
Figure 4.1	SISO System	41
Figure 4.2	PD Compensation Systems	43
Figure 4.3	Hub Angle PD Feedback System	45
Figure 4.4	Hub Angle PD Feedback Root Loci	46
Figure 4.5	Hub Angle PD + SPR Feedback System	49
Figure 4.6	SPR Open Loop System with Unmodeled Modes	54
Figure 5.1	Experimental Controller Architecture	59
Figure 5.2	Step Response Simulations	60
Figure 5.3	Step Response Simulations Closeup	60
Figure 5.4	SPR T.F. Bode Plots with R.O. Luenberger Observer	62
Figure 5.5	SPR T.F. Bode Plots with Pole Placement F.S. Observer	62
Figure 5.6	SPR T.F. Bode Plots with LQE F.S. Observer	63

Figure 5.7	Experimental Step Response with Different Observers	64
Figure 5.8	Synthesized SPR Output Comparison	65
Figure 5.9	Step Response Experimental Results	65
Figure 5.10	Step Response Experimental Results Closeup	66
Figure 5.11	Experimental Bode Plots	67

ACKNOWLEDGMENTS

I would like to thank Dr. John Wen for his continued patience, support, and ideas which are a major part of this thesis. I would also like to thank Judy Bloomingdale, Denise Elwell, Betty Lawson and Diane Brauner for their help in getting things done and Deepak Sood, Michael Repko, Steven Murphy and Chris Seaman for kindly showing me the ropes at CIRSSE.

ABSTRACT

This thesis describes the single link flexible beam testbed at the CLaMS laboratory in terms of its hardware, software and linear model and presents two controllers, each including a hub angle PD feedback compensator and one augmented by a second static gain full state feedback loop, based upon a synthesized strictly positive real (SPR) output, that increases specific flexible mode pole damping ratios w.r.t the PD only case and hence reduces unwanted residual oscillation effects. Restricting full state feedback gains so as to produce a SPR open loop transfer function ensures that the associated compensator has an infinite gain margin and a phase margin of at least $[-90, 90]$ degrees. Both experimental and simulation data are evaluated in order to compare some different observer performances when applied to the real testbed and to the linear model when uncompensated flexible modes are included.

INTRODUCTION

This thesis is organized into five chapters describing the hardware, software, modeling, control design and test results for the single link flexible manipulator system at the CLaMS laboratory. The testbed is designed so as to enable the study of the identification and control of a real flexible system and the concept is similar to that of the earlier work done by Cannon and Schmitz (see e.g., [3]).

Chapter one details the hardware which is centered on an aluminum beam (a plate), driven by a motor at one end while the other end is free, which was designed to exhibit low frequency poorly damped flexible modes. The real time controlling microprocessor is a 20 Mhz Inmos Transputer mounted on a motherboard attached to a VME backplane : analog to digital and digital to analog converter cards mounted on the same backplane provide external signal interfaces. Currently a hub angle sensor and beam strain sensors are used while two tip displacement sensors are being installed, namely a light sensor and an induction sensor.

The second chapter describes the main software functions which implement linear and non-linear controllers and run on two transputers : three controllers are designed in this thesis and each is characterized by a fixed interval discrete time linear observer and compensator pair. Also, beam parameter identification is carried out with the same software. Reference trajectories and controller parameters are loaded from Matlab data files before each experiment and afterwards the resulting data is stored in a similar fashion for later analysis. Before each experiment the D/A and A/D converter DC offsets may be loaded from another Matlab data file or updated via a short (about 25 seconds) test routine.

Chapter three outlines the linear modeling of the beam, from the governing pair of linearized partial differential equations to a finite normal mode approximation in state space form and the computation of the output sensor matrix for the hub

angle potentiometer and beam strain gages. This linear model is characterized by a collection of second order transfer functions (the beam modes) driven by a common input torque and each sensor can be viewed as a linear combination of the associated states. The rigid body mode contains a stable real pole and a pole at the origin whilst each of the others have a very poorly damped but stable complex pole pair with a unique oscillation frequency (these are called the flexible modes). The complete transfer function is thus the linear combination of the individual modal transfer functions each of which dominates close to its center frequency. A brief description of the identification process is also given : direct modal parameter identification is used.

The fourth chapter describes two full state compensators designed to improve the beam tip displacement response and each requires an observer to provide the state estimate. The first controller designed is a hub angle PD compensator which is found to give very good results in terms of tip displacement step response time, overshoot and residual oscillations. The design method used is simple : initially ignore the flexible modes and select those PD compensators which move the two rigid body mode poles such that the second order closed loop system is, say, critically damped. Then restore the flexible mode dynamics and select a single PD compensator from the previous set that also increases the flexible mode pole damping ratios with particular emphasis placed on the lowest frequency mode.

PD compensation is a form of static gain full state feedback that has the advantage of an infinite gain margin in the ideal case (i.e. perfect modeling) and this will remain true for the actual plant closed so long as the torque to estimated hub angle velocity transfer function remains strictly positive real (SPR) as is guaranteed by the Passivity Theorem. However observer, sensor and other errors will make the actual system more fragile.

The second controller designed is constructed by adding another static gain

feedback loop designed so as to further increase the damping ratios of the flexible modes. For this loop the time domain definition of strict positive realness is employed to synthesize a SPR output from the state estimate of the PD compensated plant that emphasizes selected flexible modes. By restricting the class of feedback gains in this fashion we can guarantee that static negative feedback applied to this SPR SISO system will have an infinite gain margin and a phase margin of at least $[-90, 90]$ (again in the ideal case).

The actual gains are selected through trial and error however there is a strong correlation between the improvement in individual flexible mode pole damping ratios and corresponding terms in the synthesized SPR output matrix parameterization. Two such SPR outputs are selected, one with a modal transformation applied to the PD compensated system so as to explicitly decouple the flexible modes, and the other with the original coupled PD compensated system.

Several closed loop observer designs are selected, namely a LQE full state observer, a pole placement full state observer and a reduced order Luenberger observer.

In the fifth and final chapter some simulations and experimental results are examined in order to evaluate the performance of the controller/observer combinations in step response tests. The distorting effects of the observers in conjunction with unmodeled beam modes on the synthesized SPR transfer function is examined through simulations and the observer which most faithfully reconstructs this transfer function (and performs well when applied to the true plant) is selected. Experimental bode plots are also examined since they give a good indication of flexible mode pole damping ratios.

CHAPTER 1

Hardware

1.1 Overview

Figure 1.1 is an outline of the physical single flexible link testbed the central component being the flexible beam itself which is chosen to provide readily measurable flexibility in the horizontal plane that is independent of gravity (ideally). This is driven by a DC motor at one end about a vertical axis in order to excite the flexible modes, and the other end is free. The motor is energized by a power amplifier which itself is controlled by a single voltage signal; the power amplifier-motor combination provides an approximately linear voltage to beam hub torque relationship. The hub angle is converted to a voltage signal by a potentiometer while the beam strains at specific locations are likewise converted by strain gages. The realtime computer is a networked set of four Inmos Transputer micro-processors which are connected to a PC-AT host for software development and user interface. These Transputers also connect to a VME signal bus on which resides the digital to analog (D/A) and analog to digital (A/D) circuit cards providing the motor drive (computer output) and sensor (computer input) signal interfaces.

1.2 Selecting the Flexible Beam

A problem with a single flexible plate (i.e., a thin beam) is that the unsupported end can sag due to the effect of gravity when the beam is flexed and this is a source of nonlinear behavior and an unwanted complication. To minimize this effect a high Youngs modulus to density ratio is desired in order to maximize strength and minimize weight and mainly for this reason aluminum was selected as the beam material over steel, brass or plastic (see table 1.1); this ratio is similar for both steel

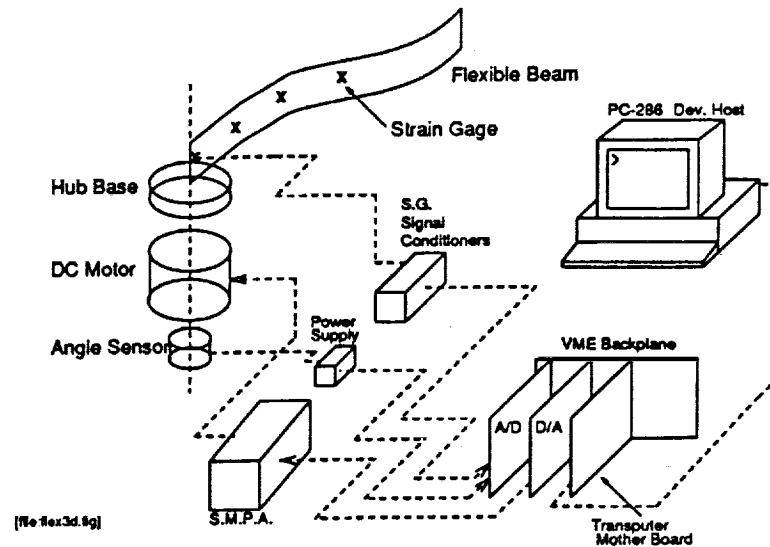


Figure 1.1: Testbed Physical System

and aluminum however the latter is much lighter and hence higher acceleration may be achieved for a given applied hub torque. Furthermore we can expect sagging to increase with a decreasing beam width or height to length ratio.

Another factor to consider is the oscillation frequencies of the beam which depend upon the material properties and the geometry of the system. For both the fixed-free (i.e. $I_h = \text{hub inertia} \rightarrow \infty$) and the pinned-free (i.e. $I_h = 0$) cases the oscillation frequencies for the linear model are of the form (see equation 3.8),

$$f_n \propto \frac{w}{L} \sqrt{\frac{E}{\rho}} \quad (1.1)$$

where,

$f_n = n_{th}$ modal frequency, $n = 0, 1, ..$

$E =$ Youngs Modulus,

$\rho =$ Density,

$L =$ Beam Length,

$w =$ Beam Width.

Table 1.1: Candidate Beam Materials

Material units	Density Kg/m^3	Youngs Mod. Kg/m^2	$\sqrt{E/\rho}$ \sqrt{m}
Aluminum, Alloy 6061.	2.713e3	6.895e10	5.041e3
Steel, Type 302.	8.028e3	1.957e11	4.937e3
Brass, CA 230.	8.748e3	1.172e11	3.660e3
Plexiglas, typical values.	1.18 e3	2.969e09	1.586e3

When the hub inertia lies somewhere between the two extremes given above the equation for f_n becomes more complex however the values for f_n will fall between those of the fixed-free and pinned-free cases.

In order to minimize the computer speed requirement low oscillation frequencies are desired and hence we wish to minimize the width to length ratio and minimize the Youngs modulus to density ratio, however this will have the effect of increasing sagging at the tip and hence a compromise is required.

A beam length of approximately one meter was chosen to provide a relatively large structure that will not be significantly affected by multiple sensors (e.g. strain gages, hub angle sensor, position light sensors) and to minimize the effects of hub shaft friction. Several beams of aluminum, steel and plastic were examined with a height of ten centimeters approximately and a width such that the fourth frequency was close to $50Hz$ and the aluminum beam was selected as it sagged the least and had a low weight.

1.3 Actuator

A DC motor and switch mode power amplifier were selected to drive the beam as this combination provides a good degree of inherent open loop linearity at a reasonable cost and is a common method of actuating robot joints. The motor is a PMI Disc DC motor which contains no rotor iron other than the central shaft (the

coils are compressed into a flat disc) and this provides four main benefits,

1. no inter-coil iron implies no cogging torque, a common unwanted non-linearity in other DC motor types,
2. the rotor mass is concentrated near the shaft axis and hence has a low inertia which yields high acceleration; in the complete setup the hub mounting is the main hub inertial component,
3. the small rotor coils have a low inductance value which increases the amplifier/motor bandwidth,
4. low coil inductance eliminates commutation brush sparking which reduces motor generated electrical noise.

The main disadvantage of this particular motor is the shaft friction torque due to brush/coil contact and the use of solid bearings.

A switch mode power amplifier, as its name implies, operates as a switch to alternatively apply full motor rotor coil voltage in one direction and then the other at a high frequency (20Khz nominal). This is obviously a highly nonlinear process however the switching process is controlled so that the motor current is nearly linearly proportional to the input voltage signal over smaller bandwidth (e.g. 1Khz) which is more than sufficient for our purposes. The only reasons for the switching operation are amplifier design considerations eg. power efficiency and component cost.

The motor/amplifier combination provides a low pass filter voltage to torque transfer function and the dominant pole location is determined by the rotor circuit resistance and inductance,

$$\tau = 1/LR \quad (1.2)$$

τ = the dominant pole time constant,

L = rotor circuit inductance,

R = rotor circuit resistance.

and is estimated to be $2msec$ approximately which means a 500 Hz bandwidth.

While the low rotor inductance is desirable in order to maximize this bandwidth it has the unfortunate effect of increasing the motor rms current which determines the heat dissipated. A small inductor was added into the rotor circuit to contain this effect doubling the overall inductance (this is included in the $500Hz$ bandwidth estimation).

1.4 Sensors

1.4.1 Hub Angle

A potentiometer was chosen for sensing the hub angle because it is cheap and because the interface circuitry is very simple (assuming an A/D converter is available). However other options exist which can provide better resolution and accuracy and less noise disturbance e.g., an optical angular encoder or a resolver and one of these will eventually replace the potentiometer.

Being an analog sensor the potentiometer has infinite resolution but its accuracy is limited by circuit and contact noise and any non-linearity in the resistive material; the former affects relative accuracy while the latter reduces absolute accuracy. Furthermore, since the A/D converters have a 12 bit word length and the potentiometer translates $+/- 180$ degrees into to the A/D full scale voltage of $+/- 10V$ the actual hub angle resolution is limited to 0.0879 degrees approximately. When the beam is at rest this corresponds to a tip displacement resolution of approximately $1.68mm$.

1.4.2 Beam Strain

Thin film strain gages are used to sense beam longitudinal strain at four points along the beam and the particular strain gages selected have the following features,

1. a small size to provide a local measurement,
2. a temperature drift coefficient to offset aluminum heat expansion,
3. capable of measuring large repeated strains.

In each case the strain gages are mounted in pairs on either side of the beam so that the resistance of one increases when the beam bends while the resistance of the other decreases; each pair forms part of a wheatstone bridge circuit and this arrangement provides good immunity to unwanted side effects such as temperature dependancies or contact potentials: the rest of the bridge circuit is comprised of two high quality matched resistors.

1.5 Computer

1.5.1 Real Time Computer

The real time computer is a network of four Inmos Transputers (see figure 2.1, only two are in use at present) which may be readily expanded in the future as processing requirements dictate. The Transputer is a single chip microprocessor which is available in several formats and we use the T800-20 model which runs at 20Mhz and is rated at 20 MIPS and 2.8 Mflops peak instruction rates. Each Transputer contains the following,

1. 32 bit CPU
2. 64 bit FPU
3. 4 Kbytes of fast static RAM
4. four 20 Mbit/sec bidirectional serial links

5. 32 bit data and memory buses and a DRAM controller

The Transputers are specifically designed for external parallel operation using the high speed serial links for interconnections and these links also connect the transputers to the host development computer and the signal interface data bus.

The transputers are also designed to facilitate multi-tasking (each separate program is called a process and high speed switching is achieved between separate processes on the same Transputer) and this constitutes a second form of parallelism. Separate processes communicate with each other through channels, not shared memory, and if the processes lie on different Transputers then these channels are mapped to the physical hardware links before runtime. In this way the code may be re-distributed across different nets by simply defining a new mapping operation and therefore the processes need not be rewritten. Thus there are two distinct networks, the real hardware form and the desired software form. Note that while any number of software channels (memory permitting) may exist between processes running on the same Transputer, this is not the case for inter-Transputer communication as each Transputer has exactly four serial links.

A third form of parallelism exists since the transputer allows the CPU, FPU and link interfaces to operate in parallel which further improves the computers performance if software is written to take advantage of this feature.

The high level parallel language Occam was developed to make optimal use of the Transputers hardware features and thus experimental control and data input/output algorithms are written in this language. The code used was originally written in MicroSoft Quick C (almost ANSI C compatible) for an PC-AT386 based system and now an Inmos ANSI C compiler is used for non-speed critical sections while the rest has been converted to Occam.

1.5.2 Development Host Computer

The user interface to the Transputers is provided by a PC-AT286 micro computer and when developing the software the Occam or ANSI C compilers and linkers are downloaded to the transputers along with the source code which then performs the compilation, linking and network configuring. At runtime the Transputers are reset and then the executable code is downloaded and booted.

1.5.3 Computer to Signal Interface

1.5.3.1 Interface Card Bus

A VMEbus was selected to interface the Transputers to the A/D and D/A cards because of its large data bandwidth and the wide variety of compatible circuit cards that exist and also because it is the bus used by an adjacent laboratory (the CIRSSE Dual Robot Arm Testbed). This bus supports 8, 16 and 32 bit data words at a maximum speed 40MHz and the backplane is mounted along with the circuit power supply in a Eurocard rack.

1.5.3.2 A/D Converters

The A/D card selected is a XVME-566 made by XYCOM and features 32 single ended, or 16 differential, input channels with 12 bit resolution and 12 bit accuracy. One channel may be sampled at a time (the conversion time is 10 μ sec) with a maximum sample throughput rate of 100Khz and any number of channels up to the maximum may be sampled in any sequence and the results stored in on board RAM.

In the current configuration single ended bipolar voltage input (+/- 10V) is used, the programmable gain is set to unity and the data ram is memory mapped to one of the Transputer microprocessors via the VMEbus so that each sample is accessed by a direct memory read command.

The inputs may be alternatively configured as 16 differential channels which should improve the signal noise common mode rejection ratio, however tests showed the measured noise to be greatly reduced when operated in single ended mode; I do not know why this is the case.

1.5.3.3 D/A Converters

The D/A card is a VMIVME-4100 made by VME Microsystems Int. Corp. and it contains eight 12 bit $\pm 10V$ output channels each of which has a settling time of $8\mu\text{sec}$ (max) to $\pm 1/2$ LSB. Like the A/D card, the data RAM is memory mapped via the VMEbus to a Transputer and may be written to directly.

CHAPTER 2

Software

2.1 Software Overview

The original computer program was written in Microsoft Quick C (almost ANSI C compatible) to run on a PC-386; C was chosen for several reasons, the main ones being,

1. it has a relatively fast compiled code execution,
2. it is the most commonly used language amongst the students
3. and faculty working in the laboratory
4. it is a flexible language capable of implementing complex data structures.

The PC-386 has now been replaced by a set of four micro-processors, the Inmos Transputers, interconnected by high speed serial data links and a host computer (a PC-286) for file handling and the user interface in order to greatly increase computation power and to facilitate further expansion if so desired; the Transputers and their links constitute the computer hardware network (see figure 2.1).

Optimum performance is obtained if software is written in the language Occam which was developed by Inmos for the Transputers and therefore the speed critical control and data I/O interface algorithms were converted to two separate processes using the Inmos Parallel Occam compiler while the rest of the original program (i.e.. the user interface and file handling section) was recast as a single process using the Inmos Parallel ANSI C compiler. The processes communicate with each other and the host through asynchronous data channels; the processes and their channel configuration constitute the software network and this is distributed amongst the hardware network as shown in figure 2.1.

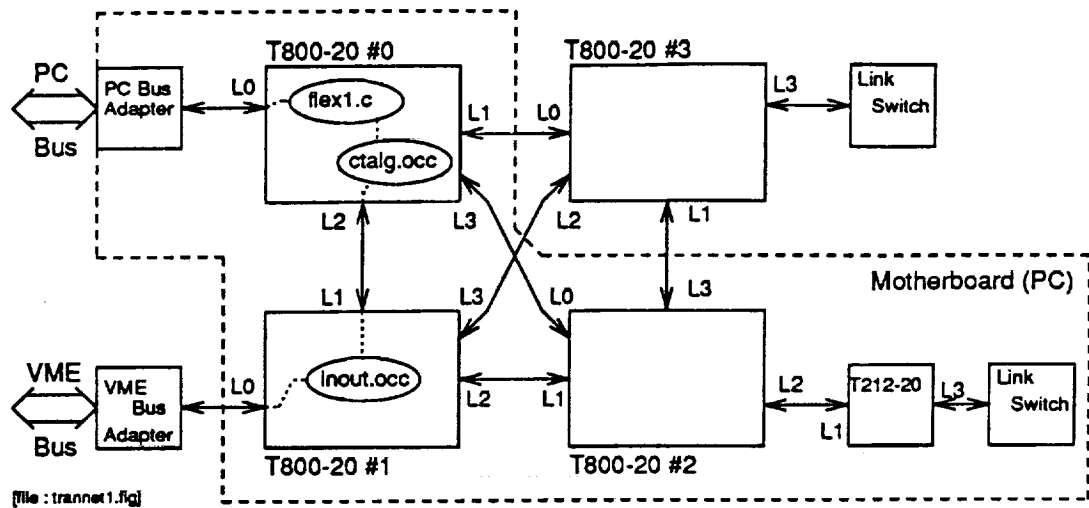


Figure 2.1: Software Flow Diagram #1 (High level)

The user and file interface process is called flex1.c and it provides data input and storage and user communication via the host computer screen and keyboard. Data files are stored in the Mathworks MATLAB .mat format to allow an easy interface with the tools of the MATLAB mathematical analysis software on either the host PC-286 or a SUN workstation network to which it is connected. Figure 2.2 shows a high function level schematic for flex1.c which emphasizes the .mat file interface and the initialization and/or resetting sequences which the testbed is put through prior to each experiment.

The process ctalg.occ implements the several realtime control algorithms used during experimentation. These are written as general discrete time state space systems and/or discrete time nonlinear operators whose parameters are configured prior to an experiment from data stored in a .mat file. Input consists of a combination of sensor feedback from the testbed and pre-defined data vectors while outputs are the actuator control signals (only one is needed to control the single link flexible beam). The two control algorithms used in this report are,

1. Open Loop Control which passes input data from a .mat file directly to the actuator channels,

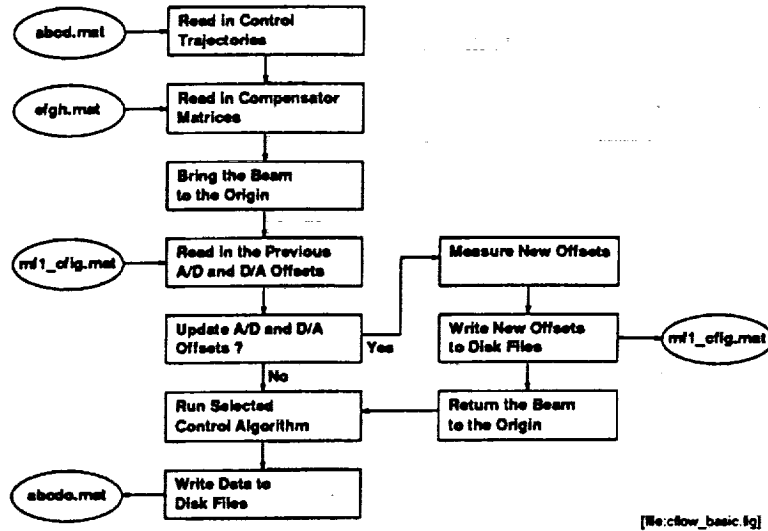


Figure 2.2: Software Flow Diagram #1 (High level)

2. Linear Observer and Feedforward Compensator.

2.2 Program Description

The main purpose of the software is to provide a set of easily configurable constant time interval sampled data controllers for the flexible beam apparatus (i.e., the "plant"), including a linear observer/feedforward compensator, with the following features (see figure 2.2),

1. Each controller has a fixed structure written in software and selectable parameters which are loaded from a .mat configuration file. Note that there is a compromise to be made between the generality of the controller and the speed of execution, e.g., the linear observer/feedforward compensator controller may be written as a more general linear controller however matrix computations increase.
2. Controller input and feedforward trajectories are stored in a .mat input file as data vectors (i.e. $1 \times n$, or $n, \times 1$ arrays where n , is the number of data

samples taken during the experiment),

3. Controller output (i.e., plant input) and plant feedback to the controller vectors are stored in a .mat output file after the experiment.
4. Plant input and output signal steady state offsets may be automatically measured prior to each experiment, stored in a .mat file, and compensated for during the experiment.
5. Both the sampling time interval t_s , and the number of samples taken during an experiment are specified in the input file.

2.3 Resetting Signal Offsets

Each analog component of the testbed hardware is subject to nominal signal changes between experiments due to temperature induced drifts, aging of components, and distortions caused by the experiments themselves (e.g., a large strain on the flexible beam can slightly bend it so that the strain gage steady state values measurably change). In order to minimize the effects of such errors the software includes an option to measure these offsets prior to the experiment and the I/O procedure then automatically compensates (by subtracting from A/D values and adding to D/A values). Furthermore the new offsets are stored in a .mat file (mfl_cfg.mat) and are used during subsequent experiments until they are measured again; in practice the offsets are usually updated prior to each experiment.

Strain gage signal offsets are measured by averaging a series of readings taken over five seconds while the beam is at rest (i.e., the input torque is at zero) while the potentiometer offset is always set to zero for experiments where the absolute zero angle is unimportant.

The offset related to the motor amplifier circuit is more problematic due to the effect of hub shaft friction. In the absence of friction the unique amplitude of

the signal applied to the power amplifier would equal the offset when the motor is at rest and hence be easily measured. However in actuality the beam will come to rest if the applied motor field torque is less than the friction dynamic threshold and remain there as long as the static threshold is not exceeded and hence zero applied torque condition is not readily detected. One solution is to apply a dither signal directly to the motor amplifier and add a proportional negative feedback loop; assuming a sufficiently large dither signal and convergence of the operating point to a periodic cycle the amplifier circuit offset will correspond to the average applied torque signal. In practice a 10Hz signal is applied and after a pause of 5 seconds the average over 5 seconds of the torque signal is calculated.

CHAPTER 3

Beam Modeling

3.1 Beam Analytical Modeling

3.1.1 Linear Differential Equations

The essential model components of the testbed are the beam itself driven by a torque at the hub, and the effective hub inertia. Figure 3.1 shows the coordinate frames and geometric notation used in the following equations. The corresponding non-linear beam model was derived in [1] using Hamilton's Principle with the following initial assumptions,

1. Hooke's Linear Stress-Strain Law holds.
2. The beam elongation is negligible.
3. The beam deformation is small.
4. The hub and bending velocities are small.

and a set of linearized partial differential equations was subsequently obtained,

$$EI_a \frac{\delta^4 v}{\delta x^4} + \rho_x \frac{\delta^2 v}{\delta t^2} = 0 \quad (3.1)$$

$$\tau - I_H \ddot{\phi} + EI_a v''(0, t) = 0 \quad (3.2)$$

with the boundary conditions

$$v(0, t) = 0, l; v'(0, t) = 0, v''(0, t) = 0, v'''(L, t) = 0,$$

E = beam material Youngs Modulus

τ = the input motor torque,

ρ_x = the beam mass per unit length,

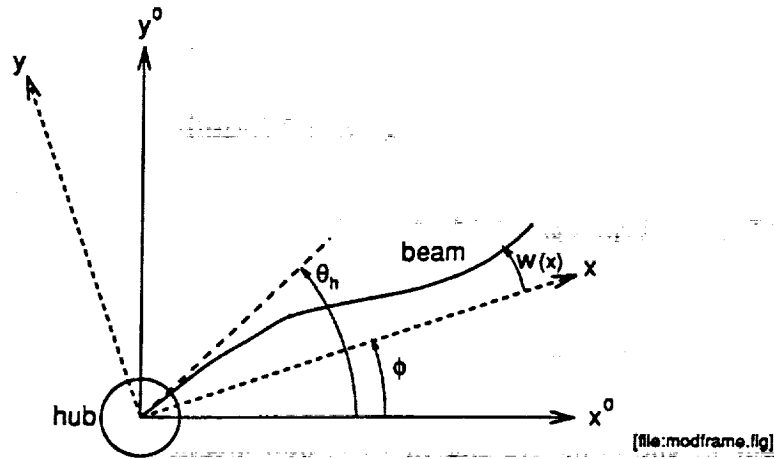


Figure 3.1: Beam Model Coordinate Frames

I_h = hub inertia,

L = the beam length,

$v = \omega + x\phi$,

ϕ = rigid body mode angle,

θ_h = the hub angle,

$w(x)$ = beam displacement at x meters along the nominal axis.

3.1.2 Normal Mode Form

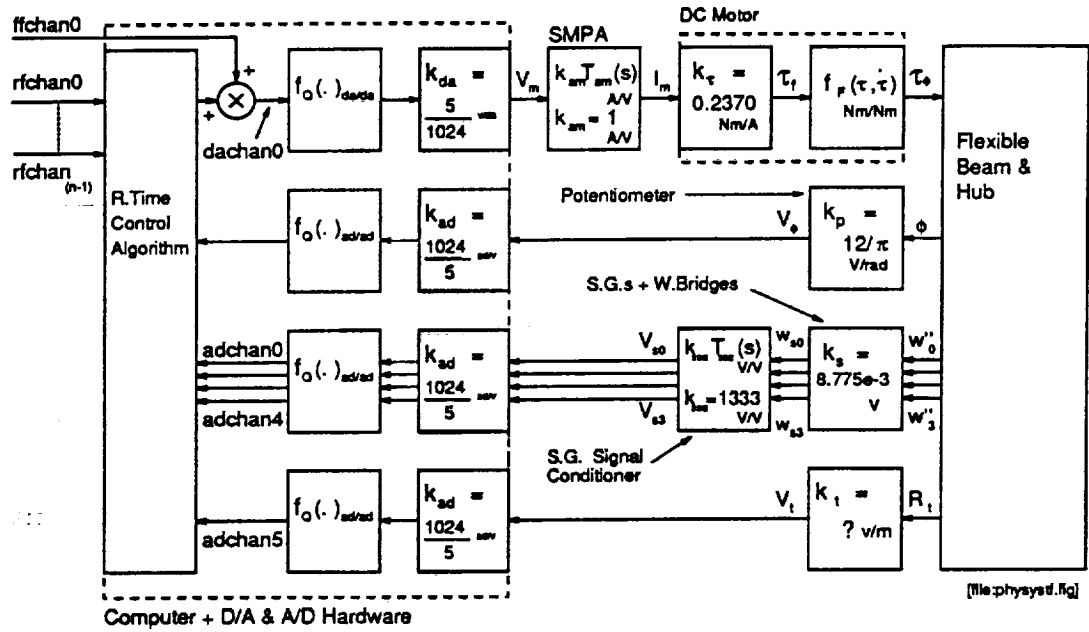
An eigen-analysis of these equations is performed in order to establish the infinite set of modal frequencies $\{w_i\}$ at which the beam exhibits resonance (damping is not included in the model at this stage) and corresponding mode shapes $\{\psi_i(x)\}$, including one rigid body mode ($w_0 = 0$, $\psi_0(x)$ = a straight line) where,

$$\psi_i(x) = A_i \sin(k_i x) + B_i \sinh(k_i x) + C_i \cos(k_i x) + D_i \cosh(k_i x) \quad (3.3)$$

$$A_i = \frac{c \operatorname{ch} + s \operatorname{sh} + 1}{-s \operatorname{ch} + c \operatorname{sh}} C_i \quad (3.4)$$

$$B_i = \frac{2\rho_x}{I_h k_i^3} C_i - A_i \quad (3.5)$$

$$D_i = -C_i \quad (3.6)$$



1. Linear model $\Rightarrow f_Q(x) = x$ and $f_F(\tau, \dot{\tau}) = \tau$.
2. Low frequencies $\Rightarrow T_{am}(s) \approx 1$ and $T_{ssc}(s) \approx 1333$.

Figure 3.2: Testbed Physical System

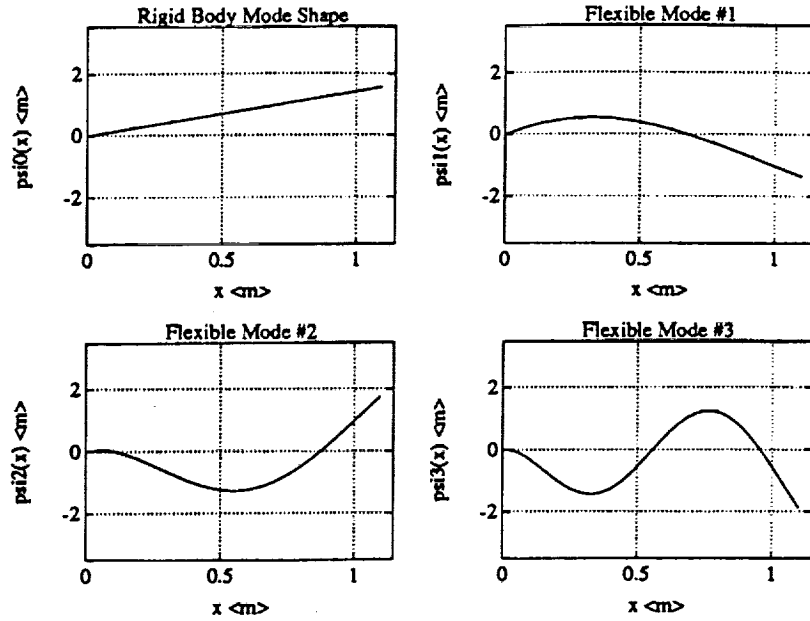


Figure 3.3: First Four Normal Mode Shapes

where $s = \sin(k_i L)$, $c = \cos(k_i L)$, $sh = \sinh(k_i L)$ and $ch = \cosh(k_i L)$

C_i may be chosen arbitrarily and may be used to scale the units of $\{\psi_i(x)\}$ (dimensions meters). $\{k_i\}$ are the set of solutions to

$$\frac{I_H}{\rho_x} k_i^3 (1 + c ch) + (s ch - c sh) = 0 \quad (3.7)$$

and the corresponding oscillation frequencies are given by,

$$\omega_i = k_i^2 \sqrt{\frac{EI_a}{\rho_x}} \quad (3.8)$$

Table 3.1 lists the first nine such frequencies for the flexible beam used (see appendix 5.3 for the material dimensions and constants) plus a zero which represents the zero k solution to equation (3.7) and the rigid body mode; figure 3.3 shows the corresponding beam mode shapes described by equation (3.3) and scaled so that each a_n is unity.

Note that the mode number is the same as the number of oscillation zeros that exist along the beam.

Table 3.1: Beam Normal Mode Parameters

i	f_i Hz	\hat{f}_i Hz	$\frac{100(f_i - \hat{f}_i)}{\hat{f}_i}$	$\frac{\psi_i'(0)}{a_i \rho_x} N^{-1} m^{-1}$	$\hat{\tau}_i$ sec	$\hat{\zeta}_i$
0	0	0		3.19	0.92	-
1	2.83	2.83	0.0	7.65	2.5	0.0229
2	7.42	7.15	3.8	4.22	1.9	0.0115
3	19.06	17.8	7.1	1.53	0.87	0.0097
4	36.99	35.4	4.5	0.768	1.7	0.0025
5	61.03	58.0	5.2	0.462	1.6	0.0016
6	91.10	90.8	0.3	0.309	0.73	0.0024
7	127.21			0.221		
8	169.34			0.166		
9	217.50			0.129		

1. i = mode number (i.e., number of mode shape nodes -1)
2. f_i = calculated mode natural frequency = $\frac{\omega_i}{2\pi}$
3. \hat{f}_i = measured mode natural frequency = $\frac{\hat{\omega}_i}{2\pi}$
4. $\hat{\tau}_i$ = measured decay time constant = $\frac{1}{\zeta_i \hat{\omega}_i}$
5. $\hat{\zeta}_i$ = measured damping ratio

Next the linearized partial differential equation solutions are obtained in terms of these modal quantities to yield $v(x, t)$, the linear approximation of the radial displacement of the beam at a distance x along the beam from the hub at time t ,

$$v(x, t) = \sum_{i=0}^{\infty} q_i(t) \psi_i(x) \quad (3.9)$$

$$\ddot{q}_i + \omega_i^2 q_i = \frac{\psi_i'(0)}{a_i \rho_x} \tau \quad (3.10)$$

where $q_i(t)$ = the i^{th} modal amplitude function ,

$$a_i = \langle \psi_i, \psi_i \rangle + \left(\frac{Ih}{\rho_x}\right) \psi_i'(0) \psi_i'(0), \quad (3.11)$$

$\langle f(x), g(x) \rangle = L_2[0, L]$, the innerproduct of $f(x)$ with $g(x)$,

The i_{th} mode is thus governed by a second order linear differential equation (3.12) which is an undamped forced harmonic oscillator. The pole damping ratio

(ζ_i) for each flexible mode is now estimated experimentally and inserted to produce,

$$\ddot{q}_i + 2\zeta_i\omega_i\dot{q}_i + \omega_i^2q_i = \frac{\psi'_i(0)}{a_i\rho_x}\tau \quad (3.12)$$

3.1.3 Finite State Space Normal Mode Approximation

The A and B matrices of a finite state space representation n modes can now be easily derived from equation (3.12) if we truncate the model after the n^{th} mode

$$\dot{x} = A_m x + B_\tau \tau \quad \text{where,} \quad (3.13)$$

$$A_m = \begin{bmatrix} 0 & 1 & 0 & 0 & \dots & 0 & 0 \\ 0 & -d_0 & 0 & 0 & \dots & 0 & 0 \\ 0 & 0 & 0 & 1 & \dots & 0 & 0 \\ 0 & 0 & -\omega_1^2 & -d_1 & \dots & 0 & 0 \\ \vdots & \vdots & \vdots & \vdots & \ddots & \vdots & \vdots \\ 0 & 0 & 0 & 0 & \dots & 0 & 1 \\ 0 & 0 & 0 & 0 & \dots & -\omega_n^2 & -d_n \end{bmatrix}, \quad B_\tau = \begin{bmatrix} 0 \\ \frac{\psi'_0(0)}{a\rho_x} \\ 0 \\ \frac{\psi'_1(0)}{a\rho_x} \\ \vdots \\ 0 \\ \frac{\psi'_n(0)}{a\rho_x} \end{bmatrix} \quad (3.14)$$

$$x = \begin{bmatrix} q_0 & \dot{q}_0 & q_1 & \dot{q}_1 & \dots & q_{n-1} & \dot{q}_{n-1} \end{bmatrix}^T \quad (3.15)$$

Currently used are a hub angle sensor (a potentiometer) and four strain gages mounted along the beam and in each case the signals produced can be approximated by a linear combination of the states $x(i)$ to produce the output C matrix, and the D matrix is null and the corresponding sensor velocities are obtained by shifting the appropriate C matrix rows one place to the right in order to meet the \dot{q}_n states.

3.2 Hub Actuator

With reference to figure 3.2 the switch mode power amplifier and DC motor dynamics may be approximated by the following linear transfer function relationship,

$$\tau(s) = k_\tau k_{am} T_{am}(s) V_m(s) \quad (3.16)$$

$$\text{where } T_{am}(s) = \frac{\tau_{am}}{s + \tau_{am}} \quad (3.17)$$

$$\text{and } k_r = \frac{\tau(s)}{I_m(s)}, \text{ the motor torque constant.} \quad (3.18)$$

Here τ_{am} is the dominant time constant of the power amplifier and DC motor field winding circuit, $T_{am}(s)$ is the associated low pass transfer function due to resistance and inductance (see chapter 1) and k_{am} is the low frequency switch mode power amplifie/DC motor voltage to motor circuit current (I_m) gain. Since τ_{am} and is estimated to be 2 milliseconds approximately; it is neglected (i.e., assumed infinite) for the purposes of this report as the highest modal frequency considered is 58Hz, and hence equation (3.17) may be approximated by

$$\tau(s) = k_r k_{am} V_m(s). \quad (3.19)$$

3.3 Hub Angle Sensor

Equation (3.13) describes the torque to modal state transfer function and we now relate the modal state to the hub angle ϕ ; the truncated form of equation (3.9) implies

$$\phi = v'(0, t) = \sum_{i=0}^n q_i(t) \psi'_i(0) \quad (3.20)$$

where $\psi'_i(0)$ is the derivative of the i^{th} mode shape at the origin (i.e., the hub shaft) and is found by differentiating equation (3.3) . Equation 3.20 can be recast in state space form as,

$$\phi = C_\phi x \quad (3.21)$$

$$C_\phi = \left[\begin{array}{cccccc} \psi'_0(0) & 0 & \psi'_1(0) & 0 & \dots & \psi'_n(0) & 0 \end{array} \right] \quad (3.22)$$

Note that C_ϕ can be related to B_r (see equation (3.14) as follows:

$$C_\phi = B_r^T P_\phi \quad (3.23)$$

where P_ϕ is a diagonal strictly positive definite matrix and since the only system pole that is not exponentially stable (i.e., the rigid body mode pole at the origin) is decoupled from the hub velocity output the Positive Realness Theorem guarantees that the torque to hub angle transfer function is strictly positive real, (see chapter 4).

3.3.1 Angle to Voltage Conversion

A single turn potentiometer is used to convert the hub angle ϕ to a voltage signal: with reference to figure 3.2

$$V_a = \phi \cdot k_p \quad \text{and} \quad k_p = \frac{V_s}{2\pi} \quad (3.24)$$

where V_s is the potentiometer supply voltage, and k_p is the conversion constant.

3.4 Beam Strain Sensors

The longitudinal strain at a specific point on the beam surface is closely related to the curvature $w''(x, t)$ of the beam at that point and we can relate the latter to the modal states in truncated form as follows,

$$w''(x, t) = v''(x, t) = \sum_{i=1}^i q_n(t) \psi_i''(x) \quad (3.25)$$

where $\psi_i''(x)$ are given by equation 3.3 and therefore in state space form,

$$w''(x, t) = C_s(x)x \quad (3.26)$$

$$C_s(x) = \left[0 \quad 0 \quad \psi_1''(x) \quad 0 \quad \dots \quad \psi_n''(x) \quad 0 \right]. \quad (3.27)$$

Note that $\psi_0(x)$ may be calculated explicitly and is found to be

$$\psi_0(x) = \sqrt{a} \left(\frac{L^3}{3} + \frac{I_H}{\rho_x} \right) x \quad (3.28)$$

and hence $\psi_0''(x)$ is zero for all x .

3.4.1 Strain Gage Geometry

The strain gages are mounted in pairs opposite to each other on either side of the beam so that together they can measure the extent of bending at a particular distance along the beam, half way up the side. (see figure 1.1). Only one strain gage is strictly necessary at each point of interest, however considerable noise and disturbance immunity is achieved by using them in pairs as one arm of a Wheatstone bridge configuration (see figure 3.6). In fact four strain gages completing the bridge circuit are even better, two mounted on each side of the beam close together, but it is not clear that the performance improvement over two is significant and worth the extra cost and construction. Figure 3.4 shows a cross section of the beam with a pair of strain gages on either side (looking down from above the beam). The important dimensions are,

d_{beam} = the width of the beam,

d_{sub} = strain gage substrate thickness,

d_{glue} = estimated glue thickness,

d_{film} = thickness of strain gage film,

$$\text{and } d_{1/2} = d_{beam}/2 + d_{glue} + d_{sub} + d_{film}/2 \quad (3.29)$$

$$\approx 7.938 \times 10^{-4} + 5 \times 10^{-7} = 8.438 \times 10^{-4} \quad (3.30)$$

is the distance between the beam neutral axis and the center of the strain gage film half the effective beam width with respect to the strain gages.

A strain gage, of the type used, is a pattern of resistive material whose resistance increases when stretched and when the beam bends in a clockwise direction (cw)(looking down from above) the cw+ strain gage is elongated and so its length undergoes positive strain (hence the name cw+), while at the same time, the cw- strain gage is forced to contract, implying negative strain. The strain gages are very linear devices over a wide range of strains and the altered resistances increase V_{sg}

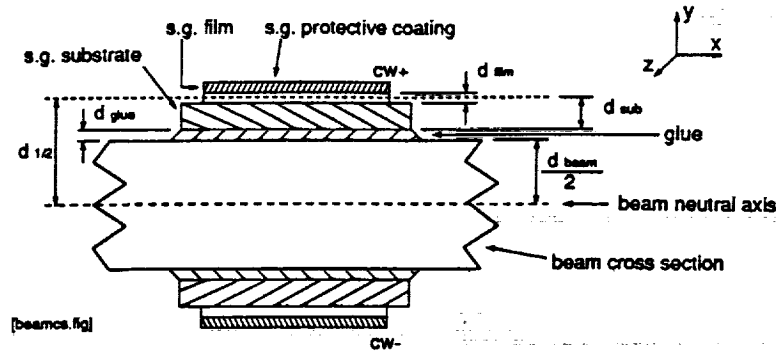


Figure 3.4: Beam and Strain Gage Cross Section

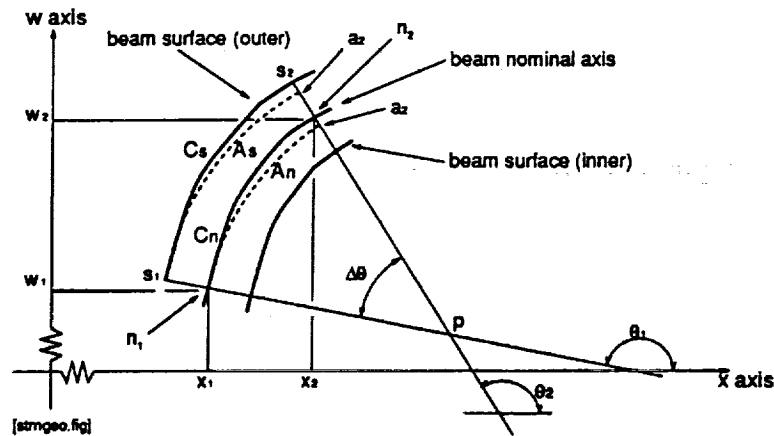


Figure 3.5: Beam Curvature Geometry

in figure 3.6 which is amplified by the strain gage signal conditioner to produce V_{so} while the opposite occurs when the beam curves the other way.

Note that the strain gages directly measure strain in the plane of the strain gage, not on the surface of the beam or elsewhere, however the strain in any plane parallel to the nominal axis plane is linearly proportional to its distance from the nominal axis plane, and hence conversion between different strains is achieved by scaling.

The quantities of interest in this project are the modal state amplitudes and we can relate these to the strains by first constructing figure 3.5, a cross sectional diagram in the $x-y$ plane of the rotating beam frame. Let x_1 an arbitrary point

along the beam neutral axis when at rest (ie. the x axis) with $w_1 (\triangleq w(x_1))$ as the nominal axis displacement associated with the linear model; $n_1 \equiv (x_1, w_1)$. Also choose x_2 such that

$$\begin{aligned} x_2 &= x_1 + \Delta x, \\ w_2 &= w(x_2) ; n_2 \equiv (x_2, w_2). \end{aligned}$$

It is assumed that Δx is chosen sufficiently small such that the segment of the n.a. C_n , ($\equiv [n_1, n_2]$), is continuously convex w.r.t. a particular side of the beam. Let A_n be the corresponding nominal axis curve section, length l_n (i.e., A_n is a circular arc centered at p and connecting n_1 to the transverse plane line through n_2). At n_1 and n_2 extend the beam transverse lines until they meet at some point p and let R_i be the length of $[n_i, p]$; θ_i is the angle between the x axis and the transverse lines. The transverse plane and outer surface intersections are labeled s_1 and s_2 and the connecting beam curve is called C_s , with a corresponding nominal axis curve section A_s .

Let

$$\theta_{ii} = \theta_i - 90 \text{ degrees}, \quad i = 1, 2 \quad (\text{then } w'_i = \tan(\theta_{ii})) \quad (3.31)$$

$$\Delta\theta \triangleq \theta_2 - \theta_1 = \theta_{i2} - \theta_{i1}, \quad (3.32)$$

$$l_{cn} = \text{length}(C_n), \quad l_{an} = \text{length}(A_n) \quad (3.33)$$

$$L_{cs} = \text{length}(C_s) = l_{cn} + \Delta l_{cs} \quad (3.34)$$

$$L_{as} = \text{length}(A_s) = l_{an} + \Delta l_{as} \quad (3.35)$$

where Δl_{cn} and Δl_{an} are the n.a. curve and arc length extensions due to strain deformation respectively.

3.4.2 Curvature-Strain Linear Relationship

The following limits are assumed

$$\lim_{\Delta x \rightarrow 0} \frac{C_n}{A_n} = 1, \quad \lim_{\Delta x \rightarrow 0} \frac{C_s}{A_s} = 1, \quad (3.36)$$

$$\lim_{\Delta x \rightarrow 0} \frac{l_{cn}}{l_{an}} = 1, \quad \lim_{\Delta x \rightarrow 0} \frac{L_{cs}}{L_{as}} = 1, \quad (3.37)$$

$$\lim_{\Delta x \rightarrow 0} \frac{\Delta l_{as}}{\Delta l_{cs}} = 1, \quad \lim_{\Delta x \rightarrow 0} \frac{\Delta x}{l_{cs}} = \cos(\theta_{t1}). \quad (3.38)$$

Now

$$R_1 \Delta \theta = l_{an}, \quad (R_1 + \frac{d_{beam}}{2}) \Delta \theta = l_{an} + \Delta l_{as}, \quad (3.39)$$

$$\Rightarrow \frac{d_{beam}}{2} \Delta \theta = \Delta l_{as} \quad (3.40)$$

and therefore

$$w'_2 - w'_1 = \sin(\Delta \theta) / (\cos(\theta_{t1}) \cos(\theta_{t2})) \quad (3.41)$$

$$\text{so, } w''_1 = \lim_{\Delta x \rightarrow 0} \frac{(w'_1 - w'_2)}{\Delta x} = \lim_{\Delta x \rightarrow 0} \frac{\sin(\Delta \theta)}{\cos(\theta_{t1}) \cos(\theta_{t2}) \Delta x} \quad (3.42)$$

$$= \frac{1}{\cos^2(\theta_{t1})} \lim_{\Delta x \rightarrow 0} \frac{\Delta \theta}{\Delta x} = \frac{1}{\frac{d_{beam}}{2} \cos^2(\theta_{t1})} \lim_{\Delta x \rightarrow 0} \frac{\Delta l_{as}}{\Delta x} \quad (3.43)$$

$$= \frac{1}{\frac{d_{beam}}{2} \cos^3(\theta_{t1})} \lim_{\Delta x \rightarrow 0} \frac{\Delta l_{as}}{l_{cs}} = \frac{1}{\frac{d_{beam}}{2} \cos^3(\theta_{t1})} \lim_{\Delta x \rightarrow 0} \frac{\Delta l_{cs}}{l_{cs}} \quad (3.44)$$

$$= \frac{1}{\frac{d_{beam}}{2} \cos^3(\theta_{t1})} \lim_{\Delta l_{cs} \rightarrow 0} \frac{\Delta l_{cs}}{l_{cs}} = \frac{e_1}{\frac{d_{beam}}{2} \cos^3(\theta_{t1})} \quad (3.45)$$

where e_1 is the beam convex surface engineering strain (and a convex surface implies that e_1 is positive). Lastly

$$e_1 \triangleq \lim_{l_{cs} \rightarrow 0} \frac{\Delta l_{cs}}{l_{cs}} \quad (3.46)$$

$$\text{and hence } e_{s1} \triangleq e_1 \frac{d_{beam}}{d_{1/2}} = w''_1 \left(\frac{d_{beam}}{2} \cos^3(\theta_{t1}) \right) \quad (3.47)$$

$$\Rightarrow w''_1 \approx \left(\frac{1}{d_{1/2}} \right) e_{s1} \quad (3.48)$$

for small deflection angles θ_{t1} where e_s is the strain experienced by the corresponding strain gage, (the strain in the opposite strain gage is equal to $-e_s$). The

term $\frac{d_{beam}}{d_{1/2}}$ is due to the fact that the active part of the strain gages are raised from the beam surface and hence the true distance from the center of the beam is larger than half the actual beam width.

3.4.3 Curvature-Strain Non-linear Relationship

Equation 3.47 is nonlinear and may be expanded as follows

$$w'_1 = \tan(\theta_{t1}) \Rightarrow \cos^2(\theta_{t1})(w'_1)^2 = (1 - \cos^2(\theta_{t1})) \quad (3.49)$$

$$\Rightarrow \cos^2(\theta_{t1}) = (1 + (w'_1)^2)^{-1} \quad (3.50)$$

$$\Rightarrow \cos^3(\theta_{t1}) = (1 + (w'_1)^2)^{-2/3} \quad (3.51)$$

$$\Rightarrow e_{s1} = \frac{\frac{d_{beam}}{2} w''_1}{(1 + (w'_1)^2)^{2/3}} \quad (3.52)$$

Assuming that $(w'_1)^2 \ll 1$, a binomial expansion implies that

$$e_{s1} = \frac{d_{beam}}{2} w''_1 (1 - 3/2(w'_1)^2 + O((w'_1)^4)) \quad (3.53)$$

and since w'_1 may be expressed in terms of the modal states

$$w'_1(t) = v'(x_1, t) - \phi(t) = \sum_{i=0}^n q_i(t) [\psi'_i(x_1) - \psi'_i(0)] \quad (3.54)$$

equation (3.48) may be modified to include a power series approximation to the nonlinear relationship up to any desired order :

$$w''_1 \approx \left(\frac{1}{d_{1/2}} \right) \frac{1}{(1 - 3/2(w'_1)^2 + O((w'_1)^4))} e_{s1}. \quad (3.55)$$

For the discrete model a previous estimate of the plant may be used in order to calculate w'_1 and this then be subsequently used in equation (3.47) for the current estimate of w''_1 . This approximate non-linear compensation is not used in simulations or experiment in this Thesis.

3.4.4 Strain to Voltage Conversion

As mentioned above two strain gages are used opposite each other at every measurement point along the beam in a wheatstone bridge circuit, (see figure 3.6). The 10V DC supply voltage (V_{sp}) is provided by the Analog Devices 3B18 signal conditioner and the bridge output (V_{sg}) feeds into this same circuit which amplifies, buffers and low pass filters the signal (see appendix 5.3). If R_{cw+} and R_{cw-} are the resistances of the strain gages cw+ and cw- respectively (see above) then the basic strain gage equations are

$$\frac{\Delta R_{cw+}}{R_{cw+}} = K e_{cw+}, \quad \frac{\Delta R_{cw-}}{R_{cw-}} = K e_{cw-} = -K e_{cw+} \quad (3.56)$$

where K = some constant dependant upon the strain gage selected and ΔR_{cw+} is the resistance change in strain gage cw+ due to strain e_{cw+} .

In figure 3.6 $R_n = R_{cw+}$ nominal = R_{cw-} nominal, and R_+ , R_- are chosen equal to R_n also so that when the beam is at rest V_s is zero. Then

$$V_1 = \frac{V_{sp}}{2}, \quad \text{and} \quad V_2 = \frac{V_{sp} R_{cw-}}{(2R_n)} \quad (3.57)$$

$$\Rightarrow V_{sg} = V_2 - V_1 = \frac{V_{sp} \Delta R_{cw+}}{(2R_n)} = \frac{-V_{sp} K}{2} \cdot e_{cw+} \quad (3.58)$$

Combining equations (3.48) and (3.58) gives (for each strain gage pair)

$$V_{sg1} = k_s \cdot w_1'' \quad (3.59)$$

$$\text{where } k_s \triangleq \frac{-V_{sp} K}{2} \cdot d_{1/2}. \quad (3.60)$$

Note that in figure 3.2 V_{sg1} is called W_{s1} . $K = 2.08$, $V_{sp} = 10$ and $d_{1/2}$ as given in equation (3.30) implies that $k_s = 8.775 \times 10^{-3}$.

3.4.5 Strain Gage Signal Conditioner

The strain gage signal conditioner contains a second order low pass filter given by

$$T_{ssc}(s) \triangleq k_{ssc} \cdot \frac{\omega_{ssc}^2}{s^2 + 2\zeta_{ssc}\omega_{ssc} + \omega_{ssc}^2}. \quad (3.61)$$

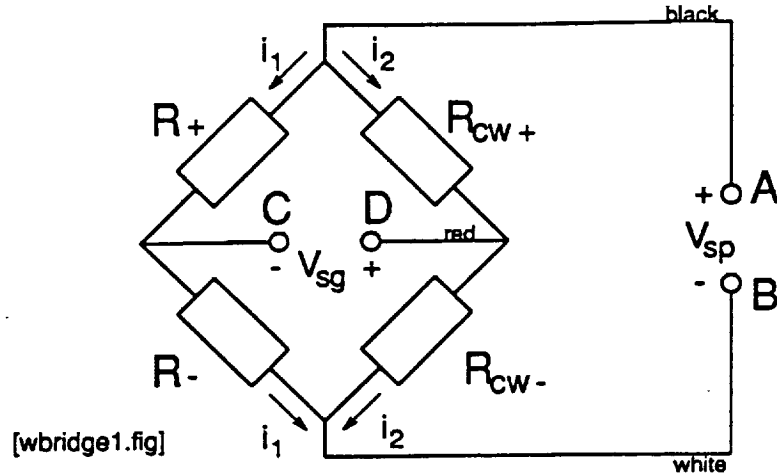


Figure 3.6: Strain Gage Wheatstone Bridge

(3.62)

Currently $k_{ssc} = 1333$, $\zeta_{ssc} = 1$ and $\omega_{ssc} = 100.2\pi$ however these dynamics are not included in the linear model used in this Thesis, rather only the low frequency approximation of $T_{ssc}(s) \approx k_{ssc}$ is used.

3.5 Computer Input and Output

Each A/D converter may be considered as a constant gain of k_{ad} (ad units)/V followed by an amplitude quantization operator $f_Q(\cdot)$, while a D/A converter is the same operator followed by a constant gain of k_{da} which is currently configured so that $k_{da} = \frac{1}{k_{ad}}$, i.e.,

$$y_{ad}(t) = f_Q(k_{ad}x_v(t)) \quad (3.63)$$

$$\text{and } y_v(t) = k_{da}f_Q(x_{da}(t)) \quad (3.64)$$

where $x_v(t)$ and $y_v(t)$ are voltage signals, and $x_{da}(t)$ and $y_{ad}(t)$ are amplitude quantized signals. $f_Q(x)$ rounds x to the nearest integer but this this quantization effect is ignored in the linear model and so

$$y_{ad}(t) = k_{ad}x_v(t), \quad (3.65)$$

$$y_v(t) = k_{da} x_{da}(t) \quad (3.66)$$

are assumed.

3.6 Complete Testbed State Space Model

With reference to figure 3.2 the separate system transfer functions may now be cascaded to produce the overall model referenced to the computer control algorithm as follows,

$$\dot{x} = Ax + Bu, \quad y = Cx \quad (3.67)$$

$$A^{2n \times 2n} = A_m \quad (3.68)$$

$$B^{2n \times 1} = B_\tau k_\tau k_a k_{da} \quad (3.69)$$

$$C^{2m \times 2n} = k_{ad} \begin{bmatrix} k_p C_\psi \\ k_p C_\psi^v \\ k_{ssc} k_s C_{s0} \\ k_{ssc} k_s C_{s0}^v \\ \vdots \\ k_{ssc} k_s C_{s4} \\ k_{ssc} k_s C_{s4}^v \end{bmatrix} \quad (3.70)$$

$$\text{where } x = \begin{bmatrix} q_0 & \dot{q}_0 & q_1 & \dot{q}_1 & \dots & q_{n-1} & \dot{q}_{n-1} \end{bmatrix}^T, \quad (3.71)$$

$$u = \text{control effort in AD units} \quad (3.72)$$

$$\text{and assuming } y = \begin{bmatrix} y_{hub} & y_{hub}^v & y_{s0} & y_{s0}^v & \dots & y_{s3} & y_{s3}^v \end{bmatrix}^T \text{ in AD units} \quad (3.73)$$

$$C_{row}^v = \begin{bmatrix} 0 & C_{row}(1, \dots, 2m-2) \end{bmatrix} \quad (3.74)$$

i.e., C_{row} shifted once to the right and with a zero inserted.

Figure (3.7) shows the bode plots for several input/output transfer functions when the first five flexible modes are included; it is emphasized that the above model, and therefore these plots, include damping information that was obtained

experimentally, however the form of the plots is invariant with respect to large estimated damping ratio errors. Note that the hub angle velocity transfer function bode phase plot is bounded by ± 90 degrees as expected because it is strictly positive real, however so is the phase plot for the first strain gage response even though the sensor is located a distance of 6.5mm away from the hub along the beam and this is explained in the next section. All the other strain gage velocity transfer functions are seen to be not positive real.

3.7 Model Structural Features

Figure (3.8) includes a schematic representation of the plant model which helps to illustrate the following points.

1. The single input torque simultaneously excites a low pass filter and several second order filters, while each sensor is a linear combination of the filter states.
2. The rigid body mode transfer function, torque to \dot{q}_0 is a passive low pass filter, $G_0(s) = s/(s + \tau)$.
3. Each flexible mode transfer function, torque to \dot{q}_n , $n > 0$, is a passive bandpass filter, $G_i(s) = 2\varepsilon_i\omega_i s/(s^2 + 2\varepsilon_i\omega_i s + \omega_i^2)$.
4. The torque to hub angle velocity transfer function is a positive linear combination of the $G_k(s)$ and hence it is minimum phase.
5. In the complete linear model, each torque to strain velocity transfer function is not strictly positive real and hence there exist negative $C_s(x)$ elements (assuming $x > 0$). In general the further the strain gage is located from the hub the "sooner" the first negative $C_s(x)$ element occurs for a given number of modeled modes or, alternatively, for a given non-zero distance from the

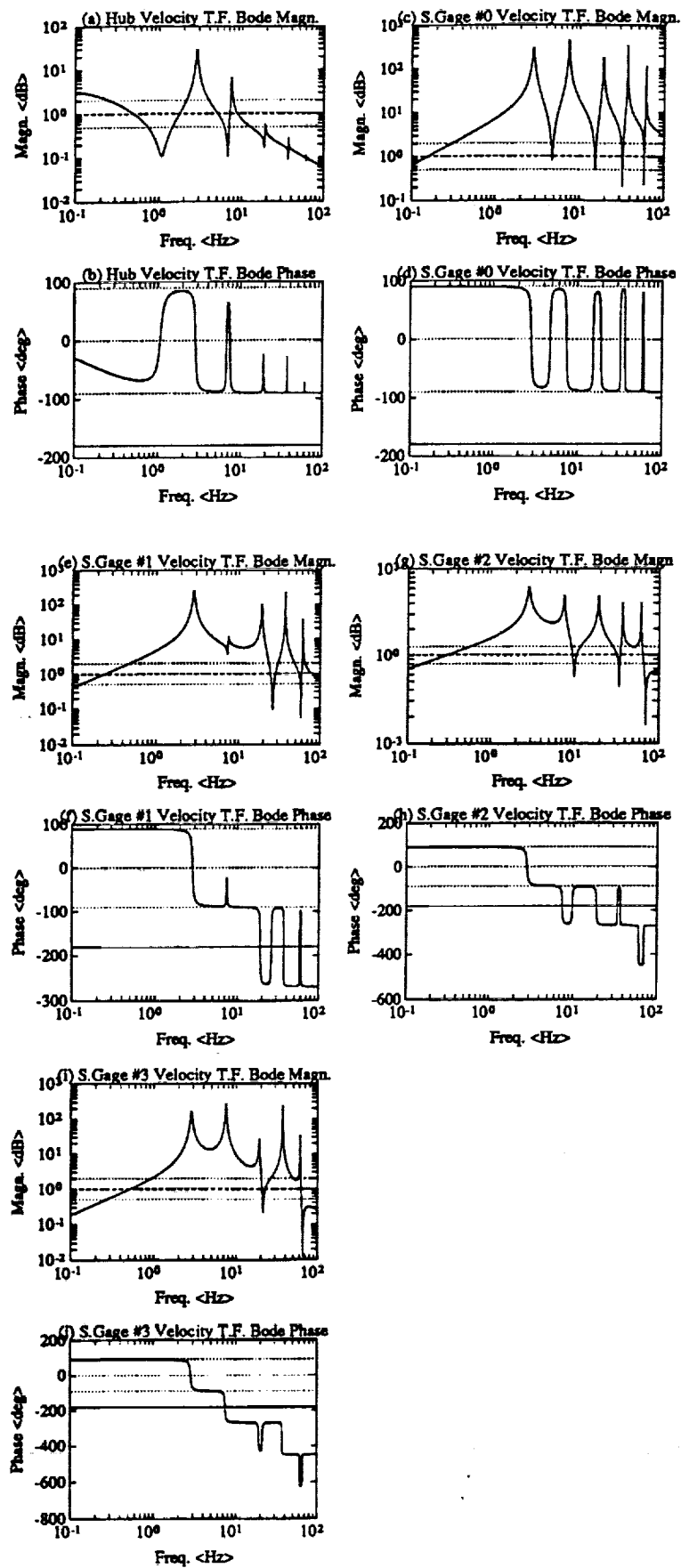


Figure 3.7: Finite Linear Model Bode Plots

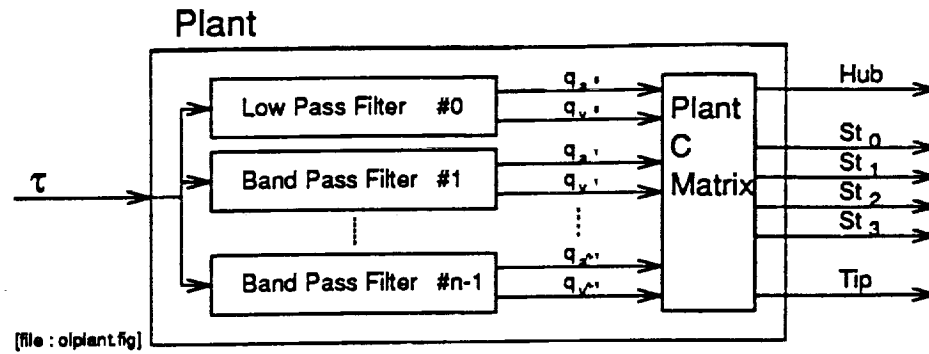


Figure 3.8: Normal Mode Linear Model Structure

origin, a negative element will occur in $C_s(x)$ for a sufficiently high order model. However, if the strain gage is close enough to the hub, $C_s(x)$ may contain only positive entries for any given number of beam modes and this is the case for the first strain gage (#0), which is only 6.5mm from the hub, and at least the first five flexible beam modes.

3.8 Model Identification

A modal analysis was carried out on the testbed in order to identify the three sets of finite linear normal mode parameters, i.e.,

1. the first n modal oscillation frequencies (\hat{f}_n),
2. the corresponding pole damping ratios ($\hat{\zeta}_n$),
3. the corresponding input/output gains for each sensor

and the results for \hat{f}_i and $\hat{\zeta}_i$ are shown in table 3.1 for $0 \leq i \leq 5$. Modal analysis was used since the test signals may be selected to target individual parameters of interest, e.g., a sinusoid at a specific flexible mode frequency produces a response strongly dominated by the corresponding flexible mode and the input/output gains may now be directly determined. The identified model parameters are considered

more accurate than the analytically derived ones from the beam and hub assembly physical parameters since some of the latter are only known approximately however the analytically derived input/output gains are used in the final model (i.e., the model used for controller design and analysis in the next chapters) since the identified input/output gain data is not up to date.

3.8.1 Oscillation Frequencies

The first step was to apply a narrowband test signal such as a PRBN function to the beam and obtain an FFT of any sensor response (although the strain gages are preferred as the oscillation peaks are well defined) and hence a set of bode plots. Since each mode is very poorly damped the shape of the sinusoidal response of a sensor close to an oscillation frequency is strongly determined by the corresponding modal transfer function and hence the experimentally obtained bode magnitude plot peak locations determine the oscillation frequencies (and hence the associated pole magnitudes). A second refined bode magnitude plot was then obtained by applying individual sinusoids at frequencies close to the estimated pole magnitudes and then the latter were re-evaluated.

3.8.2 Damping coefficients

The rigid body mode non-zero pole was measured by applying a rectangular input torque and curve fitting the hub angle response in order to determine the rate of exponential increase (a rectangle rather than a step signal was used since the latter would of course cause the beam to wind out of its operating envelope). This mode does not affect the strain gage responses and hence the corresponding strain gage data cannot be used in order to estimate rigid body mode parameters.

In order to measure the i^{th} flexible mode pole damping ratio (ζ_i) a sinusoid was applied at the corresponding center frequency ($\hat{\omega}_i$) until a steady state situation was

reached and then abruptly removed at time t_1 ; the envelope of each sensor response after t_1 exponentially decays with a time constant $\hat{\tau}_i$ given by

$$\hat{\tau}_i = \frac{1}{\hat{\zeta}_i \hat{\omega}_i} \quad (3.75)$$

and once τ_i is measured by curve fitting this envelope ζ_i may be calculated since ω_i is known.

3.8.3 Modal Gains

This last set of data also yields the input/output gains $\hat{b}_i \hat{c}_{i,j}$ for each sensor j at each oscillation frequency $\hat{\omega}_i$ from which the state space model B and C matrices may be formed.

3.8.4 Identification Improvements

The above procedures may be improved in order to more accurately identify system modal parameters and some ideas are as follows.

1. A discrete fourier transform is an estimate of the continuous fourier transform at specific discrete frequencies that are determined by the data sampling rate and the number of samples. This suggests that a better narrowband signal than PRBN would be one composed of equal amounts of sinusoids at the discrete fourier series frequencies with a random constant phase shift applied to each sinusoid in order to reduce coherent peaks in the time domain signal: unlike PRBN this signal does not waste energy on frequencies other than those assumed by the discrete fourier transform (and therefore those of interest) and provides equal weights for all frequencies. Furthermore, the amplitude weights may be accurately altered if desired, perhaps to increase the measurement signal/noise ratio at frequencies close to plant transmission zeros and any number of sinuoids may be omitted in order to precisely tailor the applied signal bandwidth. This test signal was used for the Bode plots shown in figure 5.11 which are much smoother than those obtained with PRBN

test signals. It may also be possible to specify the individual sinusoid constant phase shifts rather than set them randomly in order to minimize the maximum test signal peak in the time domain so as to further avoid nonlinear response effects associated with large input signals.

2. Estimate the coulomb friction and include corresponding nonlinear compensation during the identification process. This is particularly important since test data show significant nonlinear effects when small signals are applied to the beam and these are assumed to be due to coulomb friction. Furthermore, very large applied signals also result in nonlinear effects due to nonlinear damping, stiffening and gravity/torsion effects which may be more easily avoided if smaller signals are allowed.

3. Calculating complex pole damping ratios by analysing sinusoid decay envelopes can be difficult due to nonlinear effects that add unwanted frequencies to the data and one possibility is to filter the data with a linear second order band-pass filter centered at the same modal center frequency first and then the modal damping ratio may be derived from the measured value and that of the bandpass filter: the center frequency for such a filter is known exactly since it corresponds to the applied sinusoid frequency. Another option is to filter the data in a nonlinear manner by applying a window to the corresponding discrete fourier series to select those frequencies close to the modal center frequency and then transform back to the time domain in order to analyse the decay envelope : the decaying sinusoid fourier transform is dominated by frequencies close to its center frequency.

4. The rigid body mode non-zero pole was identified with a rectangular test signal which excites the flexible modes also and though this was taken into account a better result might be obtained by using a smoother signal, perhaps a rectangular pulse with parabolic ramping or filtered with a sharp roll off low pass filter.

CHAPTER 4

Control Design

4.1 Overview

The linear modal flexible beam model developed in chapter three (see equation (3.67)) possesses a simple decoupled structure, i.e., a collection of second order systems (a single rigid body mode and the set of flexible modes) driven by a common input torque. The rigid body mode largely determines the step response time while the flexible modes govern the oscillatory behavior and applying feedback control can decrease the step response time (i.e., move the rigid body mode real poles away from the origin in the Laplace s domain) and increase the flexible mode damping ratios (i.e., swing the flexible mode complex pair poles towards the negative real axis in the Laplace s domain). Applying any amount of hub angle proportional feedback moves the pole at the origin and the new closed loop system becomes completely controllable and observable, hence full state feedback may be used to arbitrarily place the closed loop poles. However in reality noise, non-linearities and modeling errors limit the extent to which feedback may be applied and the problem now is how to select a robust feedback controller.

A useful design tool is the Passivity Theorem (see reference [4]) which guarantees that strictly positive real feedback compensation of a positive real (m inputs and m outputs) plant will produce an asymptotically stable closed loop positive real system even in the presence of modeling errors, so long as there are no pole-zero cancellations, and furthermore such a compensator will have an infinite gain margin when applied to the plant model. In the case of the flexible beam a natural choice for a positive real (with respect to the input torque) output is the time derivative of the hub angle which may be obtained with an appropriate sensor, direct filtering

of the hub angle, or reconstructed from an estimation of the plant states (i.e. using a closed loop observer). The Passivity theorem may now be applied to show that hub angle proportional plus derivative (PD) feedback produces an asymptotically stable closed loop positive real system with an infinite compensator gain margin. This is the basis of the first controller designed and root locus analysis is used in a systematic fashion in order to select the actual proportional and derivative gains as a compromise between rigid body mode performance, flexible mode performance and pole location sensitivity to gain variations.

However the second and higher order flexible modes are only weakly observable through the hub angle sensor and in order to substantially increase the damping ratios of these modes requires unacceptably high PD gains. A solution to this problem is to synthesize a new positive real output signal, either directly from several plant sensors (collocated and/or non-collocated) or via an estimate of the PD compensated plant states, that is strongly coupled to the modes of interest and then apply a second positive real compensator (see figure 4.5). The Positive Realness Theorem provides a means for constructing such an output from the PD compensated plant states and a second controller is designed this way that improves the damping ratios on the second and third flexible modes using static feedback; a third controller tested uses a positive real filter in the feedback loop in order decouple the dynamics of higher order uncompensated modes.

Each of these controllers is designed using a four mode plant model (eight states) and an observer to provide an estimate of the plant states from which positive real outputs are generated. The effect of some unmodeled higher order modes on the positive realness of synthesized plant outputs is examined (through simulations) with different closed loop observer types, namely, full order pole placement, reduced order Luenberger pole placement and LQE designs and the observer which produces an output least sensitive to the modeling error is selected: open loop observers are

not tested.

When designing and testing compensators a mixed analytical/identified model was used since the identified model parameters are considered more accurate than the analytically ones derived from the beam and hub assembly physical parameters (see chapter 3).

4.2 Positive Realness

With reference to [2], assume a minimal (controllable and observable) exponentially stable system Σ with time domain representation

$$\begin{aligned}\dot{x}(t) &= Ax(t) + Bu(t), & x(0) &= x_0 \\ y(t) &= Cx(t) + Du(t)\end{aligned}\tag{4.1}$$

and frequency domain representation

$$y(s) = (D + C(sI - A)^{-1}B)u(s) = T(s)\tag{4.2}$$

where $x \in \mathfrak{R}^n$, $u, y \in \mathfrak{R}^m$ and $\sigma_{\min}(B) > 0$.

Theorem 1a :

(A, B, C, D) is Strictly Positive Real if there exists $P > 0$, $P, L \in \mathfrak{R}^{n \times n}$, $\mu_{\min}(L) \triangleq \epsilon > 0$, $Q \in \mathfrak{R}^{m \times n}$, and $W \in \mathfrak{R}^{m \times m}$ that satisfy the Lur'e equations

$$A^T P + PA = -Q^T Q - L\tag{4.3}$$

$$B^T P - C = W^T Q\tag{4.4}$$

$$W^T W = D + D^T.\tag{4.5}$$

For the flexible beam model (3.67) D is null and so we may take W and Q to be null in which case the above three equations reduce to

$$A^T P + PA = -L\tag{4.6}$$

$$C = B^T P.\tag{4.7}$$

This theorem offers a method of computing an output matrix C in terms of L such that the corresponding system is positive real as follows : equation 4.6 is a Lyapunov matrix equations and since $\mu_{max}(A) < 0$ (e.g., Σ is a minimal exponentially stable system) there exists a unique solution P for any given L (see [5], page 574) which may be expressed as

$$P = \int_0^{\infty} e^{A^T t} L e^{A t} \quad (4.8)$$

Furthermore,

$$L > 0 \text{ and } L^* = L \Rightarrow P > 0 \text{ and } P^* = P. \quad (4.9)$$

Therefore $B^T P(sI - A)^{-1} B$ will be a positive real transfer function if L is restricted as in 4.9. In practice equation 4.8 is not suitable for computer computation but other more efficient methods exist and are readily available (e.g., the LYAP function in MATLAB).

Physically, L determines the convergence rate of the Lyapunov function $V(x) \triangleq x^* P x$ w.r.t. the open loop plant since

$$\frac{d}{dt} V(x(t)) = -x^*(t) L x(t) \quad (4.10)$$

along any solution trajectory of $\dot{x} = Ax$.

Now, if D is null, the equivalent frequency domain conditions for positive realness are:

Theorem 2b : $T(s)$ is Strictly Positive Real if for all $\omega \in \mathfrak{R}$

$$T(j\omega) + T^*(j\omega) > 0 \quad (4.11)$$

$$\text{and } \lim_{\omega \rightarrow \infty} \omega^2 (T(j\omega) + T^*(j\omega)) > 0 \quad (4.12)$$

Hence a Nyquist plot for a positive real transfer function will lie in the closed right half complex plane while a bode phase plot will be bounded by ± 90 deg. All

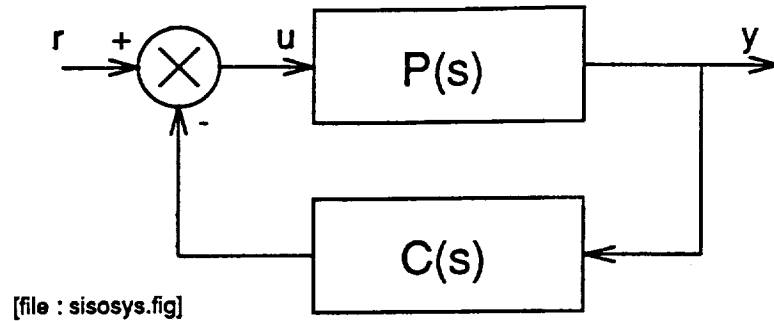


Figure 4.1: SISO System

minimum phase first order filters, such as $P_0(s)$, are positive real and so are second order bandpass transfer functions, such as $P_n(s)$. Furthermore,

$$P_i(s) \text{ positive real and } C_i \text{ positive constants for all } i \in \{0, 1, \dots, (n-1)\}$$

$$\Rightarrow \operatorname{Re} \sum_{i=0}^{n-1} P_i(s)C_i = \sum_{i=0}^{n-1} C_i[\operatorname{Re} P_i(s)] \geq 0 \Rightarrow \sum_{i=0}^{n-1} P_i(s)C_i \text{ is positive real, (4.13)}$$

i.e., positive linear combinations preserve positive realness. Since the hub angle velocity output of the flexible beam linear model is a positive linear combination of the modal velocity states (themselves positive real outputs, in fact strictly positive real outputs, with respect to the input torque) the torque to hub angle velocity transfer function is positive real. A similar result is true for strict positive realness.

4.3 The Passivity Theorem

With reference to figure 4.1

Theorem 3:

If $P(s)$ is positive real and $C(s)$ is strictly positive real then

$$T(s) \triangleq P(s)(sI - C(s)P(s))^{-1} \text{ is BIBO stable.}$$

Furthermore, if there are no unstable pole zero cancellations then

$T(s)$ is internally asymptotically stable.

This is a particular case of the Passivity Theorem and can be applied in the case of hub angle PD negative feedback for the flexible beam to guarantee closed

loop asymptotic stability assuming a non-zero derivative gain and more generally any collocated actuator and velocity sensor pair will produce a positive real transfer function for a mechanical structure that includes no energy sources.

Note that the Passivity Theorem is sufficient but not necessary; less restrictive conditions based upon the open loop plant may be developed from the Nyquist stability criterion which is itself a necessary condition.

4.4 Hub Angle PD Compensator

The hub angle forward path PD compensator is designed in two stages; firstly only the rigid body mode of the plant is modeled and a two column matrix of increasing PD gains is obtained analytically corresponding to increasing closed loop step response performance. Secondly the modeled flexible modes are included and a particular pair of PD gains is selected based on the characteristic equation root locus plot. While pole location sensitivities w.r.t. compensator parameters are also considered no attempt is made to analytically or numerically optimize a performance and/or robustness index.

4.4.1 Closed Loop Stability

Figure 4.2 (a) shows the flexible beam plant (torque to hub angle) with a PD feedback compensator. By transferring the plant integrator to the compensator block as in part (b) of the figure the modified plant becomes strictly positive real while the compensator becomes positive real (and strictly positive real for $d > 0$) and hence the Passivity Theorem guarantees asymptotic stability of the the closed loop system.

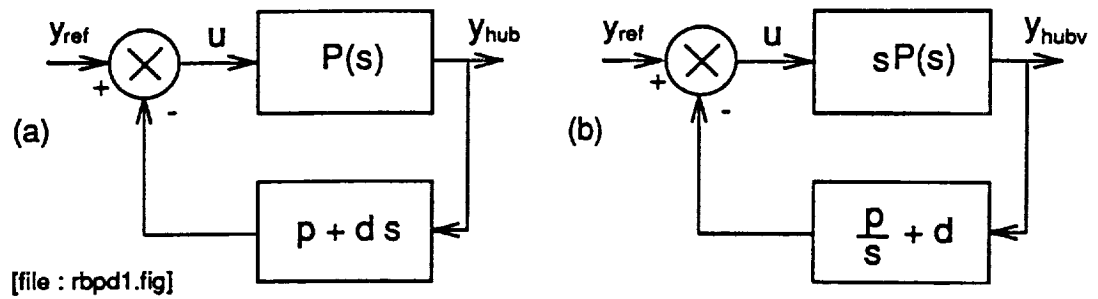


Figure 4.2: PD Compensation Systems

4.4.2 Rigid Body Mode Plant

Consider the closed loop transfer function of figure 4.3 when only the rigid body mode is included in the plant model (i.e. the flexible mode transfer functions are null), then

$$T_{rpd}(s) \triangleq \frac{P_r(s)C_{pd}(s)}{1 + P_r(s)C_{pd}(s)} \triangleq \frac{n_T(s)}{d_T(s)} = \frac{a(p + ds)}{s^2 + s(b + ad) + ap} \quad (4.14)$$

$$\text{since } C_{pd}(s) = p + ds \quad (4.15)$$

where $a > 0$, $b > 0$, $p > 0$, $d > 0$ and a and b are taken from the plant analytical model.

In order to configure $T_{rpd}(s)$ for a good step response we select the p and d gains as follows; let

$$\omega_r^2 = ap, \quad (4.16)$$

$$2\zeta_r\omega_r = b + ad, \quad (4.17)$$

where ω_r is the pole pair frequency and ζ_r their damping ratio.

Fix $\zeta_r = 1$ to ensure critical damping and select a set of increasingly large ω_r over a range of interest (e.g. $0.5 \rightarrow 4Hz$ and converted to rad/sec) and composed into a vector,

$$\vec{\omega}_r = [\omega_{r1} \ \omega_{r2} \ \dots \ \omega_{rn}] \quad (4.18)$$

then equations 4.16 and 4.17 imply that

$$p_i = \frac{\omega_{ri}^2}{a} \quad (4.19)$$

$$d_i = \frac{2\zeta_r \omega_{ri} - b}{a} \quad (4.20)$$

$$\text{and } \hat{p} = \begin{bmatrix} p_1 & p_2 & \dots & p_n \end{bmatrix}, \quad (4.21)$$

$$\text{and } \hat{d} = \begin{bmatrix} d_1 & d_2 & \dots & d_n \end{bmatrix} \quad (4.22)$$

where \hat{p} and \hat{d} are the $n \times 2$ P and D monotonically increasing gains which correspond to $\hat{\omega}_r$. The higher the values of p_i and d_i the higher is ω_{ri} and the faster the closed loop step response. Note that the minimum ω_{ri} considered (i.e., for $i = 1$) is determined by equation (4.20) as

$$\omega_{r1} = \frac{b}{2\zeta_r} \quad (4.23)$$

in order to avoid any negative values for d_i since this may result an unstable $T_{rpd}(s)$.

4.4.3 Root Locus Design

The second step is to add the flexible modes to the plant model to produce $P(s)$ as shown in figure 4.3 while maintaining the rigid body mode PD compensator class subject to the constraints of equations (4.19) and (4.20) so that the new torque to hub angle transfer function $T_{pd}(s)$ is given by,

$$T_{pd}(s) = \frac{P(s)}{1 + P(s)C_{pd}(s)} = \frac{n_T(s)}{d_T(s)} \quad (4.24)$$

and the PD compensator may be expressed as

$$u = r - (p.B_{shift}^T + d.B^T)x \quad (4.25)$$

$$\text{since } y_{hub} = B_{shift}^T x \quad \text{and} \quad y_{hubv} \triangleq \dot{y}_{hub} = B^T x \quad (4.26)$$

$$\text{where } B_{shift}^T \triangleq \begin{bmatrix} B(2) & B(3) & \dots & B(n) & 0 \end{bmatrix} \quad (4.27)$$

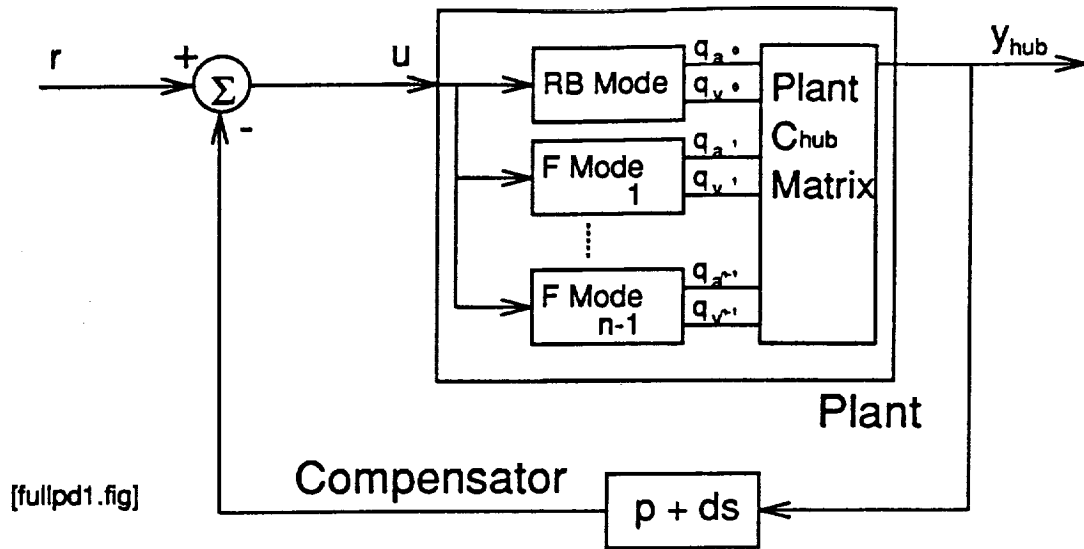


Figure 4.3: Hub Angle PD Feedback System

In the following the first two flexible modes are considered and adding these extra plant states (four in all) will not destroy the closed loop system stability as the torque to hub velocity plant transfer function remains strictly positive real.

A root locus analysis of $d_T(s)$ yields the trace shown in figure 4.4 (the left plot is a more detailed view of the right plot close to the origin) where each open loop pole is marked with an \times and the root loci emerge from these. In these root locii plots the proportional and differential gains are varied in tandem over the elements of \hat{p} and \hat{d} but the underlying parameter being varied is the desired rigid body mode closed loop pole pair frequency, ω_{ri} . The rigid body mode poles commence at $s = 0$ and $s = -a$ and proceed to move along the LHS real axis while the first flexible mode complex pole pair arc towards the real axis until they meet, travel towards the origin and then separate at a lower frequency and arc back towards the imaginary axis. The second flexible mode complex pole pair move in a less dramatic but similar manner; the pole damping ratio increases to a maximum (by a factor of three approximately) before decreasing as the poles return towards the imaginary axis with the pole frequency decreasing slowly.

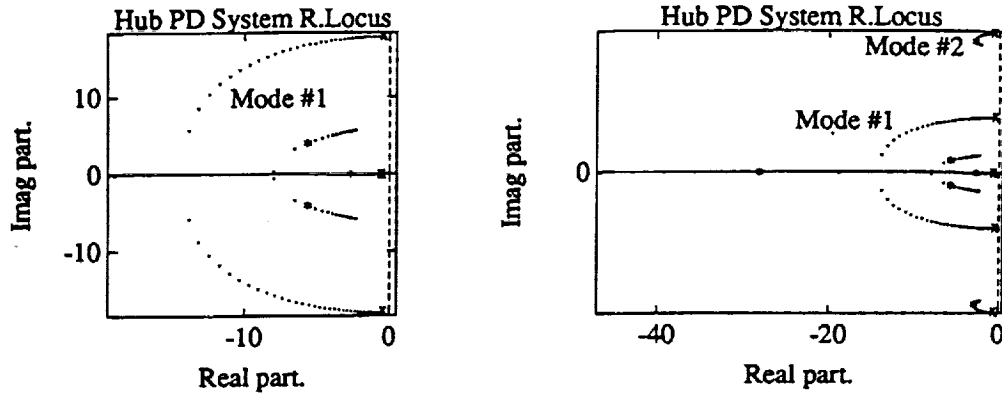


Figure 4.4: Hub Angle PD Feedback Root Loci

Table 4.1: PD Compensator Gains

p	d
2.472	1.287

An indication of the flexible mode pole sensitivity to changes in the proportional and derivative gains is the density of root loci points which is very low in the case of the first flexible mode when the poles are on or near the real axis and for this reason the corresponding P and D gains are avoided. The final pole locations were selected as a compromise between maximizing the rigid body mode performance as indicated by the magnitude of the smallest real axis pole and minimizing the first flexible mode sensitivity to gain changes as well as maximizing its pole damping ratio (and hence minimizing its associated decay time constant). Both the open loop and closed loop pole parameters are given in table 4.2 (as well as those for the next controller which includes a second feedback loop) and the PD gains used are listed in table 4.1.

The first flexible mode poles have a damping ratio close to $1/2$, a natural

Table 4.2: Compensator Pole Parameters

Mode #	f_{ol}	f_{pd}	f_{spr}	ζ_{ol}	ζ_{pd}	ζ_{spr}	τ_{ol}	τ_{pd}	τ_{spr}
0							0.92	0.38	0.40
1	2.83	1.10	1.06	0.0229	0.81	0.77	2.5	0.18	0.19
2	7.15	6.77	6.71	0.0115	0.066	0.133	1.9	0.35	0.18
3	17.8	17.8	17.7	0.0097	0.0143	0.029	0.87	0.63	0.31
4	35.4	35.4	35.2	0.0025	0.0032	0.0026	1.7	1.41	1.74
5	58.0	58.0	57.9	0.0016	0.0017	0.0013	1.6	1.62	2.12

1. subscript ol \Rightarrow open loop plant parameter,
subscript pd \Rightarrow PD compensated system parameter,
subscript spr \Rightarrow PD + SPR compensated system parameter.
2. $\tau_{xx} = \frac{1}{2\pi f_{xx} \zeta_{xx}}$

frequency of 1.1Hz, and the slowest real axis pole has a time constant of 1.85 seconds. This closed loop complex pole pair will thus have some step response overshoot, but most of this will occur during the step rise time dictated by the slow real axis pole.

The pole trajectories for the second flexible mode indicate relatively small gain sensitivity and less dramatic changes in damping ratios though for the selected p_i and d_i values their damping ratio has also increased by a factor of six approximately. Higher order modes show a progressively smaller increase in the damping ratios.

The time domain state space representation, Σ_{pd} for this closed loop system is as follows (assuming direct access to the states)

$$\dot{x} = A_{pd}x + Bu \quad (4.28)$$

$$\text{where } A_{pd} = A - B.p.B_{shift}^T - B.d.B^T \quad (4.29)$$

While A is in beam modal form (see equation (3.14)) A_{pd} will have terms coupling the beam modes together and hence is not in beam modal form.

4.5 Synthesized Positive Real Output Controller (static feedback)

The hub angle PD compensation feedback loop designed above is a form of full state feedback that provides good rigid body mode response with little or no overshoot, approximately critically damps the first flexible mode and offers an infinite gain margin in the exact model case. However the higher order closed loop flexible modes remain relatively poorly damped (see table 4.1) and in order to add further damping to these flexible modes we can modify the PD full state feedback gains by closing a second feedback loop ; the following gain selection approach makes use of the time domain state space representation definition of strict positive realness in order to guarantee an infinite gain margin and a phase margin of $[-90, 90]$ degrees for this second loop. In this example the exact gains are selected through trial and error, however there is a strong correlation between individual gain magnitudes (in a parametric form) and the corresponding closed loop flexible mode damping ratios which simplifies the selection process.

Theorem 1a implies that open loop system $P_{spr}(s) \triangleq B^T P X_{pd}(s)$ (where $X_{pd}(s) \triangleq (sI - A_{pd})^{-1} B$) will be a strictly positive real transfer function (and SISO since B is a column vector) if the square matrix P is the unique solution to

$$A_{pd}^T P + P A_{pd} = -L \quad (4.30)$$

where $L > 0$ and $L^* = L$

and the Passivity Theorem then guarantees that the close loop system $T_{spr}(s) \triangleq P_{spr}(s)[I + P_{spr}(s)]^{-1}$ will be BIBO stable with an infinite gain margin.

With regards to figure 4.5 $X_{pd}(s)$ is the torque reference ($r(s)$) to PD compensated plant state vector transfer function and $C_{SPR1} \triangleq B^T P$ is the output matrix synthesized specifically for this system so as to produce the SPR SISO transfer function $P_{spr}(s)$, and since only static negative feedback is applied the corresponding closed loop system $T_{spr}(s)$ will have a phase margin of at least $[-90, 90]$ degrees.

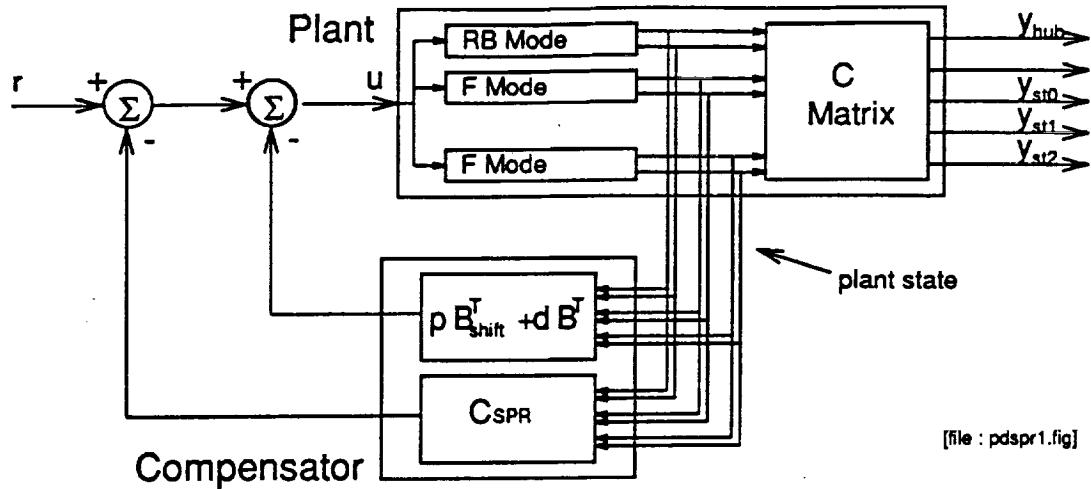


Figure 4.5: Hub Angle PD + SPR Feedback System

The effect of this second loop is to apply negative feedback that can effect the damping ratios associated with the new closed loop beam modes and we would now like to choose L so as to emphasize the poorly damped modes of Σ_{pd} through the output matrix C_{spr1} . However, since there exists coupling between beam modes (i.e. A_{pd} is not in beam modal form due to the PD feedback terms) it is immediately clear how to do so. One solution is to convert Σ_{pd} to beam modal form using a similarity transformation, solve the Lyapunov matrix equation for a new positive real output matrix using this decoupled system and then transform the output matrix to suit the original state space.

$$\text{Let } \dot{\bar{x}} = \bar{A}_{pd}\bar{x} + \bar{B}u \quad (4.31)$$

$$\text{and } \bar{A}_{pd}^T \bar{P} + \bar{P} \bar{A}_{pd} = -\bar{L}, \quad \bar{L} > 0 \text{ and } \bar{L}^* = \bar{L}, \quad (4.32)$$

where $x = M\bar{x}$, $\bar{A}_{pd} = M^{-1}A_{pd}M$, $\bar{B} = M^{-1}B$ and M is nonsingular : then

$$\bar{B}^T \bar{P} (sI - \bar{A}_{pd})^{-1} \bar{B} = B^T (M^{-T} \bar{P} M^{-1}) (sI - A_{pd})^{-1} B \quad (4.33)$$

$$\text{since } y = \bar{B}^T \bar{P} \bar{x} = B^T (M^{-T} \bar{P} M^{-1}) x \quad (4.34)$$

and the RHS of equation (4.33) is a SPR transfer function since the Positive Realness Theorem guarantees that the LHS is a SPR transfer function. Hence we

can design a SPR output matrix $\bar{B}^T \bar{P}$ by applying the Lyapunov matrix equation to the PD compensated plant in a transformed state space representation and then derive the equivalent SPR output matrix $C_{sprd} \triangleq B^T(M^{-T} \bar{P} M^{-1})$ for the original state space representation.

Now if M is chosen so that \bar{A}_{pd} is in beam modal form and \bar{L} also restricted to the same block diagonal form then equation (4.31) shows that \bar{P} will likewise be decoupled, i.e., if

$$\bar{A}_{pd} = \begin{bmatrix} a_1 & 0 & \dots & 0 \\ 0 & a_2 & \dots & 0 \\ \vdots & \vdots & \ddots & \vdots \\ 0 & 0 & \dots & a_k \end{bmatrix}, \quad \bar{L} = \begin{bmatrix} \alpha_1 l_1 & 0 & \dots & 0 \\ 0 & \alpha_2 l_2 & \dots & 0 \\ \vdots & \vdots & \ddots & \vdots \\ 0 & 0 & \dots & \alpha_k l_k \end{bmatrix}, \quad (4.35)$$

$$\bar{B} = \begin{bmatrix} b_1^T & b_2^T & \dots & b_k^T \end{bmatrix}^T, \quad a_i, l_i \in \mathfrak{R}^{2 \times 2}, b_i \in \mathfrak{R}^{2 \times 1} \quad (4.36)$$

$l_i > 0$, $l_i^* = l_i$, and $\alpha_i > 0$ are scalars

$$\text{then } \bar{P} = \begin{bmatrix} p_1 & 0 & \dots & 0 \\ 0 & p_2 & \dots & 0 \\ \vdots & \vdots & \ddots & \vdots \\ 0 & 0 & \dots & p_k \end{bmatrix}, \quad p_i \in \mathfrak{R}^{2 \times 2} \quad (4.37)$$

$$\text{where } a_i^T \alpha_i p_i + \alpha_i p_i a_i = -\alpha_i l_i \quad (4.38)$$

$$\text{and } B^T(M^{-T} \bar{P} M^{-1})(sI - A_{pd})^{-1} B \\ = \sum_{i=1}^{i=k} \alpha_i b_i^T p_i (sI - a_i)^{-1} b_i \quad (4.39)$$

and $i \in \{0, \dots, k_1\}$. The RHS of equation (4.39) shows that the contribution to the s.p.r. transfer function $B^T(M^{-T} \bar{P} M^{-1})(sI - A_{pd})^{-1} B$ by the i^{th} beam mode SPR transfer function $b_i^T p_i (sI - a_i)^{-1} b_i$ is scaled by the positive constant α_i which may be selected as desired while the form of l_i determines the relative weighting each of the two states associated with the same beam mode.

Table 4.3: Lyapunov Equation relative Weights

	α_0/α_0	α_1/α_0	α_2/α_0	α_3/α_0
Coupled L	1	20	60	80
Decoupled L	1	1	26	6

We now have two new compensators

$$u = r - (p.B_{shift}^T + d.B^T + C_{spr})x \quad (4.40)$$

$$C_{spr} \triangleq B^T P \quad (4.41)$$

$$\text{and } u = r - (p.B_{shift}^T + d.B^T + C_{SPRd})x \quad (4.42)$$

$$C_{sprd} \triangleq B^T (M^{-T} \bar{P} M^{-1}) \quad (4.43)$$

where P is the solution to the Lyapunov matrix 4.30 and \bar{P} is the solution to the decoupled form (4.31) and an example of each is selected in the following paragraphs.

4.5.1 Selecting C_{sprd} (decoupled version)

In order to emphasize the third and fourth PD closed loop beam modes several \bar{L} matrices were tested with l_i the \mathfrak{R}^2 identity matrix and α_3 and α_4 large w.r.t. α_1 and α_2 . Increasing for example α_3 increased the feedback gains associated with the third beam mode and the corresponding closed loop mode damping ratio ; in this way the set of α_i shown in table 4.3 were selected so as to increase the closed loop damping ratios of the third and fourth beam modes by a factor of approximately two over those of the PD compensated case while only slightly altering those of the first and second beam modes. The new closed loop pole parameters are not shown but are very similar to those given in table 4.2 for the PD+SPR case.

4.5.2 Selecting C_{spr} (coupled version)

For the SPR output design based upon the original coupled system Σ_{PD} the form of L chosen was that of \bar{L} in the previous example (i.e., as in equation (4.35) with l ; the \mathcal{R}^2 identity matrix) with again small values for α_1 and α_2 and large values for α_3 and α_4 . Although there is no longer an exact correlation between α_i and the contribution of each beam mode of Σ_{PD} to the synthesized SPR output there is an approximate effect if the intermodal coupling is small as is the case for the third and higher order flexible beam modes. Again α_3 and α_4 were selected so as to increase the closed loop damping ratios of the third and fourth beam modes by a factor of approximately two over those of the PD compensated case while only slightly altering those of the first and second beam modes and the results are shown in table 4.2 while the relative values for α_i are given in table 4.3

4.6 State Estimation

The experimental testbed currently contains a hub angle sensor and four beam strain gages : any other output such as a velocity signal or a synthesized passive output must be obtained by direct filtering of the existing outputs or reconstructed from an observer estimate of the plant states. The latter was chosen so as to provide a complete plant state estimate from which any desired output may be generated. Under ideal conditions a close match may be obtained between the actual and estimated state within the bandwidth of the observer, however modeling errors and unmodeled features can distort the estimated state and in this section we look at such effects due to several uncompensated beam modes (i.e., some higher order beam modes not modeled at the compensator design stage) in the presence of three different types of closed loop observers. In particular, we apply PD negative feedback based upon the estimated state of k_1 beam modes and then examine the transfer function from the single torque reference signal to the single synthesized

SPR output (as designed in the previous section) in the presence of k_2 extra beam modes not modeled when the observer and compensation were designed. The three observer designs used are 1. full state pole placement, 2. full state LQE and 3. reduced order Luenberger.

An open loop observer using an inverted plant output matrix based upon existing sensors cannot reconstruct plant velocity states since they are decoupled from these output while bandpass or highpass filtering of the existing outputs require relatively fast poles (in order to minimize the associated phase shifts) and hence will amplify high frequency noise. A closed loop observer however may reconstruct the plant velocity states (as well as amplitude states) with poles placed close to the highest modal frequencies of interest while maintaining a low phase estimate error.

In the following the observers and compensators will be designed using a beam model of k_1 beam modes and then tested with a beam model of $k_1 + k_2$ beam modes (see figure 4.6) and therefore it will be useful to partition the plant model as follows;

$$\begin{bmatrix} \dot{x}_1 \\ \dot{x}_2 \end{bmatrix} = \begin{bmatrix} A_1 & 0 \\ 0 & A_2 \end{bmatrix} \begin{bmatrix} x_1 \\ x_2 \end{bmatrix} + \begin{bmatrix} B_1 \\ B_2 \end{bmatrix} u \quad (4.44)$$

$$y = \begin{bmatrix} C_1 & C_2 \end{bmatrix} \begin{bmatrix} x_1 \\ x_2 \end{bmatrix} \quad (4.45)$$

where $A_1 \in \mathbb{R}^{2k_1 \times 2k_1}$, $A_2 \in \mathbb{R}^{2k_2 \times 2k_2}$, $B_1 \in \mathbb{R}^{2k_1 \times 1}$, $B_2 \in \mathbb{R}^{2k_2 \times 1}$, $C_1 \in \mathbb{R}^{p \times 2k_1}$, $C_2 \in \mathbb{R}^{p \times 2k_2}$, $u \in \mathbb{R}$ is the torque input signal and $y \in \mathbb{R}^p$ is the plant output vector: $[A_1, B_1, C_1]$ is the k_1 beam mode compensated system while $[A_2, B_2, C_2]$ represents the extra beam modes unmodeled at the observer/compensator design stage.

The PD negative feedback is a form of full state feedback, i.e.

$$u = r - K_{pd} \hat{x}_1 \quad (4.46)$$

$$\text{where } K_{pd} = p.B_{shift}^T + d.B^T \quad (\text{see equation (4.27)}), \quad (4.47)$$

\hat{x}_1 is the observer estimate of x_1 and r is the torque reference signal. The

Equations (4.51), (4.44) and (4.46) imply that

$$y_{pr}(s) = C_{spr}\hat{x}_1(s) = C_{spr}T_{1pd}(s)r(s) + C_{spr}T_{ei}(s)e(s) \quad (4.52)$$

$$\text{where } T_{1pd}(s) \triangleq (sI - A_{1pd})^{-1}B_1, \quad (4.53)$$

$$T_{ei}(s) \triangleq I + (sI - A_{1pd})^{-1}B_1K_{pd}, \quad (4.54)$$

$$\text{and } A_{1pd} \triangleq A_1 - B_1K_{pd}. \quad (4.55)$$

$T_{1pd}(s)$ is the designed PD closed loop transfer function (torque reference to modeled plant state) while $T_{em}(s)e(s)$ represents the associated (e)rror dynamics for the (i)deal case which in the absence of unmodeled beam modes will be exponentially stable and decoupled from v since equations (4.49) and (4.51) show that

$$\dot{e} = A_0e \quad (4.56)$$

$$\text{where } A_0 \triangleq A_1 + LC_1. \quad (4.57)$$

Now when unmodeled beam modes are included in the plant e is driven by the extra plant states x_2 and the corresponding error equation is given by

$$\dot{e} = A_0e - LC_2x_2 \quad (4.58)$$

$$\text{or } e(s) = -T_{uef}(s)x_2(s), \quad (4.59)$$

$$\text{where } T_{uef}(s) = (sI - A_0)^{-1}LC_2. \quad (4.60)$$

$$(4.61)$$

T_{uef} is the transfer function between the (u)nmodeled plant states and the modelled state (e)rror vector for the (f)ull state observer case.

Lastly, combining equations (4.59), (4.46) and (4.52) yields

$$C_{spr}\hat{x}_1(s) = C_{spr}T_{1pd}(s)[I + (I - T_a(s)K_{pd})^{-1}T_a(s)K_{pd}]r(s) \quad (4.62)$$

$$\text{where } T_a(s) = T_{ei}(s)T_{uef}(s)T_{2pd}(s) \quad (4.63)$$

and $T_{2pd}(s)$ is the unmodeled state counterpart to $T_{1pd}(s)$

$$\text{i.e. } T_{2pd}(s) = (sI - A_{2pd})^{-1}B_2 \quad (4.64)$$

$$\text{where } A_{2pd} = A_2 - B_2K_{pd} \quad (4.65)$$

Equation (4.62) shows the effect of the unmodeled dynamics (i.e., $T_{2pd}(s)$) on the synthesized positive real output $C_{spr}\hat{x}_1(s)$ (which of course may no longer be strictly positive real): if $T_{2pd}(s)$ is null then this equation reduces to the ideal case (i.e. equation 4.52 with zero error initial conditions). It is desirable to maintain the positive realness of $C_{spr}\hat{x}_1(s)$ in order to preserve the associated obtainable gain and phase margins when this second feedback loop is closed and hence equation (4.62) suggests that L and C_{spr} be selected so as to maximize

$$\inf_{\omega \in \mathbb{R}} \text{Re}(C_{spr}T_{1pd}(j\omega)[I + (I - T_a(j\omega)K_{pd})^{-1}T_a(j\omega)K_{pd}]r(j\omega)) \quad (4.66)$$

(as well as to meet other observer design criteria and emphasize selected beam modes).

4.6.2 Reduced Order (Luenberger) Observer with Uncompensated Modes Effects

The reduced order (Luenberger) observer may be represented by

$$\dot{z}_1 = A_{ro}z_1 + Eu + Gy \quad (4.67)$$

$$\hat{x}_1 = \begin{bmatrix} C_1 \\ T \end{bmatrix}^{-1} \begin{bmatrix} y \\ z \end{bmatrix} \quad (4.68)$$

$$\text{where } A_{ro}T = TA_1 - GC_1, \quad (4.69)$$

$$E = TB_1 \quad (4.70)$$

and T is also constrained such that $\begin{bmatrix} C_1 \\ T \end{bmatrix}$ is nonsingular.

The analysis of the previous section may be carried out in order to determine the transfer function relating the torque reference $r(s)$ to the synthesized SPR output

$C_{spr}\hat{x}_1(s)$ with only one change, namely the relationship between x_2 and e . Unlike the full state observer case the term $\hat{x}_1(s)$ does not appear explicitly in the reduced order observer state equations so we work with the linear combinations that do, namely $C_1\hat{x}_1(s)$ ($= y$) and $T\hat{x}_1(s)$ ($= z$) and relate these to e and then equation (4.68) gives the desired transfer function.

$$C_1\hat{x}_1 = y = C_1x_1 + C_2x_2 \quad (4.71)$$

$$\Rightarrow C_1e = C_2x_2 \quad (4.72)$$

and equations (4.67), (4.69), (4.70) and 4.51 imply that

$$Te = \dot{z} - T\dot{\hat{x}}_1 = A_{ro}Te + GC_2x_2 \quad (4.73)$$

$$Te(s) = (sI - A_{ro})^{-1}GC_2x_2 \quad (4.74)$$

Combining (4.51), (4.68), (4.72) and (4.74) gives

$$e(s) = \begin{bmatrix} C_1 \\ T \end{bmatrix}^{-1} \begin{bmatrix} C_1e(s) \\ Te(s) \end{bmatrix} \quad (4.75)$$

$$= \begin{bmatrix} C_1 \\ T \end{bmatrix}^{-1} \begin{bmatrix} I \\ (sI - A_{ro})^{-1}G \end{bmatrix} C_2x_2(s) \triangleq T_{uer}(s)x_2(s). \quad (4.76)$$

$T_{uer}(s)$ (r for (r)educed order Luenberger observer) may now replace $T_{uef}(s)$ in equation (4.62) above to give the new $r(s)$ to $C_{spr}\hat{x}_1(s)$ transfer function when the unmodeled beam modes are included.

CHAPTER 5

Simulation and Experimental Results

In the previous chapter two controllers were developed for the analytical linear model of the flexible beam, PD and PD plus synthesized strictly positive real feedback, and in the following section the step responses of the corresponding closed loop systems are examined using both linear model simulations and experimental tests on the actual testbed (and therefore in the presence of unmodeled linear and non-linear dynamics and noise). Also, distortion effects under the three closed loop observers are evaluated and the best observer selected.

The compensators and observers are converted to discrete form using the bilinear Tustin transformation and a sampling frequency of $500Hz$ which is over twenty five times higher than the highest compensated beam modal frequency : the same discretized models are used for both computer simulations and experimental tests. In each case reference trajectories are applied in the form of open loop plant modal states.

In each case the closed loop system structure is very similar to that of the open loop plant; e.g., the hub angle PD and passivity based feedback systems contain a rigid body mode (though there is no longer a pole at the origin) and flexible modes with new center frequencies and damping ratios.

5.1 Simulation Results with Ideal Observer

The PD full state controller designed in the previous chapter provides a good rigid body mode response and large damping for the Second closed loop flexible mode. However higher order closed loop flexible beam modes remain poorly damped and a second feedback loop based upon a synthesized strictly positive real output is used to increase the corresponding damping ratios by a factor of two approximately

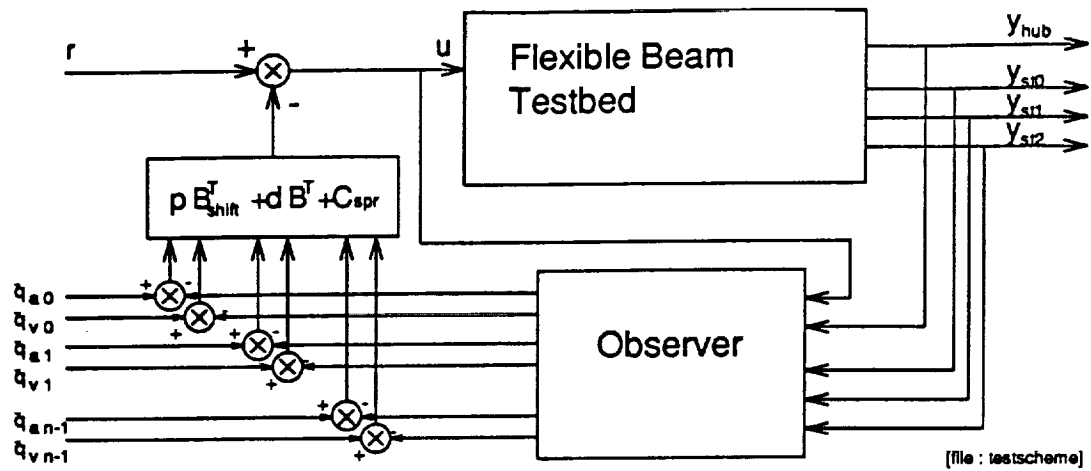


Figure 5.1: Experimental Controller Architecture

for the second and third flexible beam modes. In the absence of observer effects the differences between the two examples of these SPR based feedback are negligible and hence only the first version will be considered in this section.

Figure 5.2 shows the hub angle (a), first strain gage (b) and tip displacement (c) step responses (simulated) for the two controllers (PD and PD + S.P.R.) with a reference step size of 45 degrees. The hub angle and tip displacement 90% rise times are similar for each controller (approximately 1.8 seconds) since these are dominated by the closed loop rigid body and first flexible beam modes which are similar for both controllers. An increase in damping for the second and third flexible beam modes is evident in the strain gage plot for the PD + S.P.R controlled system which shows less residual oscillations. Figure 5.3 is another view of the first strain gage (a) and tip responses (b) starting at $t = 4$ seconds that more clearly shows residual oscillations due to closed loop flexible modes : again the PD + S.P.R controller results in greater damping.

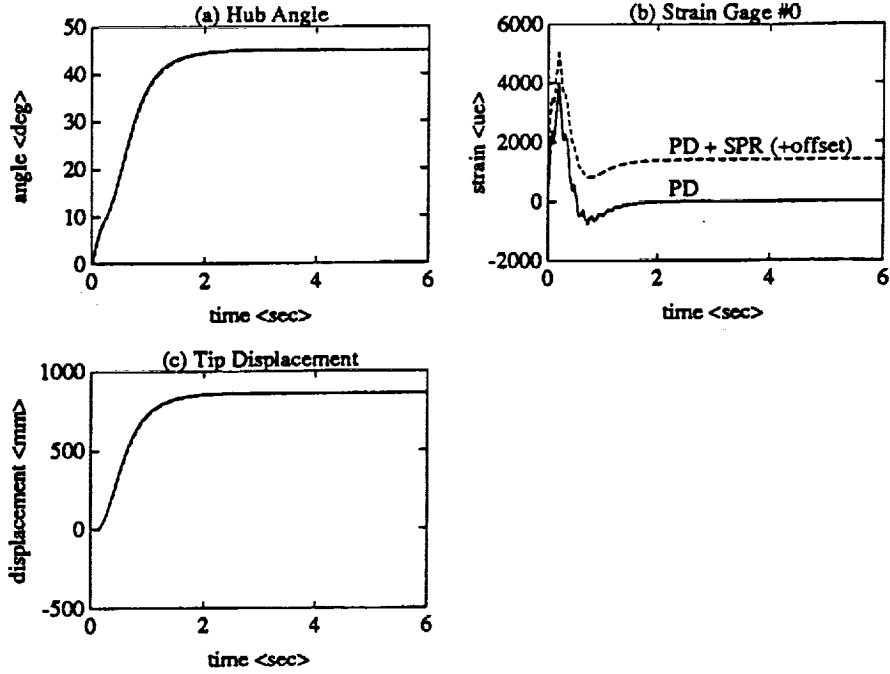


Figure 5.2: Step Response Simulations

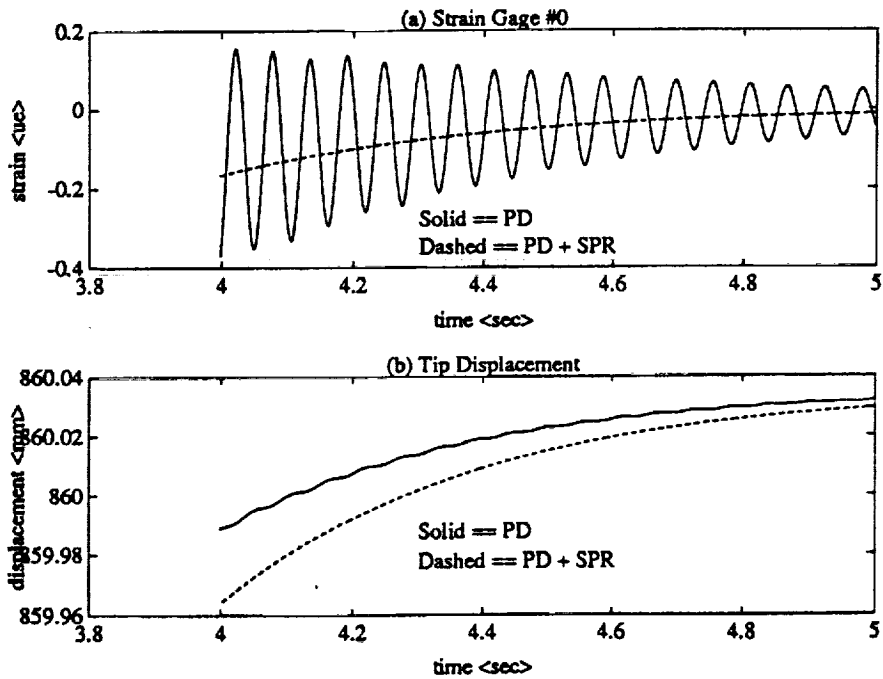


Figure 5.3: Step Response Simulations Closeup

5.2 Closed Loop Observers Effects

When observer and unmodeled beam modal dynamics are added to the computer simulations the actual transfer function from torque reference to synthesized SPR output, $\hat{T}_{1pd}(s) \triangleq C_{spr}\hat{x}_1(s)/r(s)$ (see equation (4.62)), differs from the ideal one, $T_{1pd}(s)$ (see equation (4.53)) and these non-ideal transfer functions are compared in figures 5.4, 5.5 and 5.6 to $T_{1pd}(s)$. For each of the three closed loop observers selected the error $\hat{T}_{1pd}(s) - T_{1pd}(s)$ is large in the bandwidth of the unmodeled modes and a large phase shift (much greater than -90 degrees) also occurs which means that $\hat{T}_{1pd}(s)$ is no longer SPR: in fact phase shifts greater than -180 degrees occur with gain magnitudes larger than unity and hence the stability of the closed loop system is no longer guaranteed.

Within the bandwidth of the compensated plant each observer results in a different transfer function error with the reduced order Luenberger model providing the best match, the LQE designed full state observer the worst match and the pole placement full state observer coming somewhere in between.

Figure 5.7 shows the experimental hub angle and first strain gage step responses for each of the three observer cases tested (using a PD + SPR controller) and the reduced order Luenberger and full state pole placement models produce the best results (they are almost identical to each other). The hub reference plot is shown as a dashed line. Because of the good results obtained with the reduced order Luenberger observer both in simulation and experiment it is the only one used in the next section when comparing controllers, however it is emphasized that each observer was designed through trial and error and hence we cannot conclude from these results that one observer type is categorically 'better' than another in the presence of unmodeled beam modes and other model mismatches.

The transfer function error $\hat{T}_{1pd}(s) - T_{1pd}(s)$ also depends on the selected synthesized SPR output and figure 5.8 compares $\hat{T}_{1pd}(s)$ to $T_{1pd}(s)$ for two different

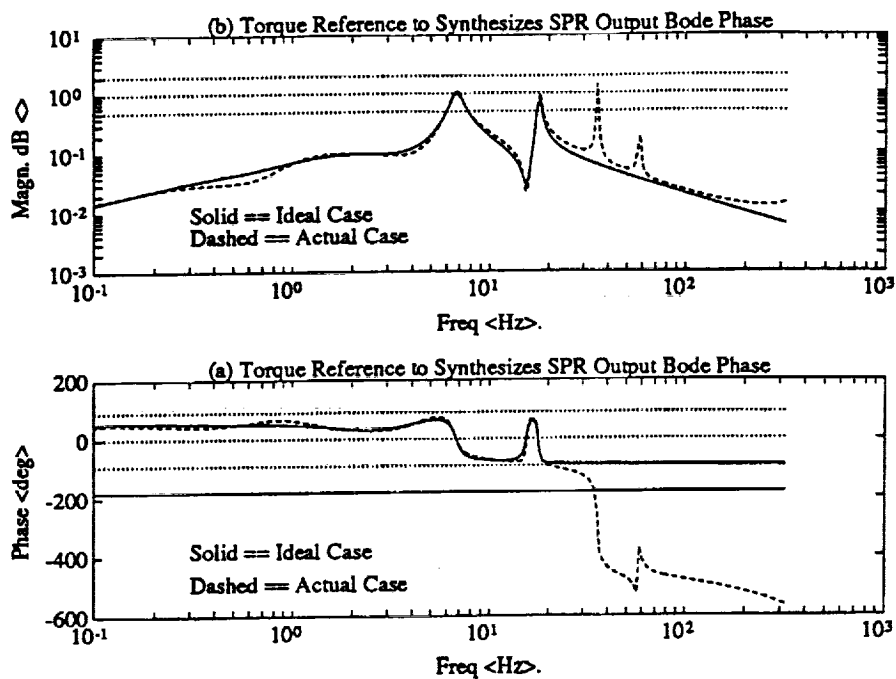


Figure 5.4: SPR T.F. Bode Plots with R.O. Luenberger Observer

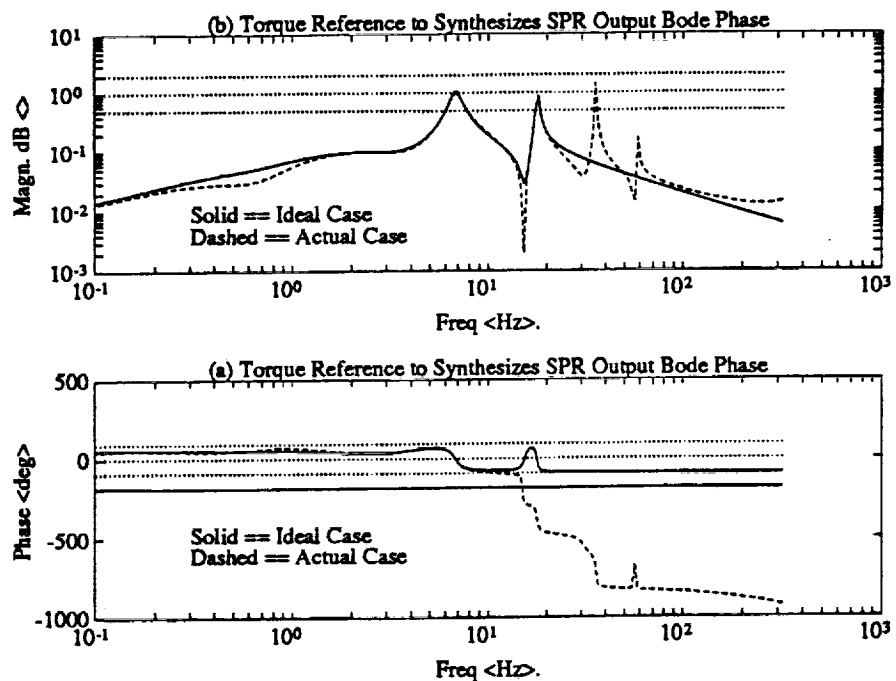


Figure 5.5: SPR T.F. Bode Plots with Pole Placement F.S. Observer

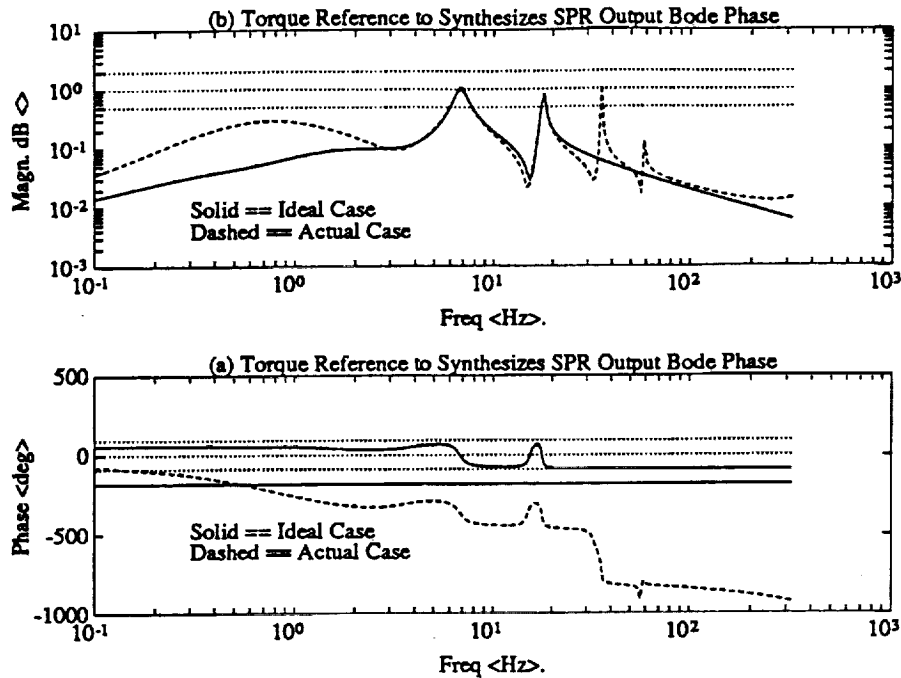


Figure 5.6: SPR T.F. Bode Plots with LQE F.S. Observer

such outputs; one design uses the PD closed loop plant in coupled form while the other used the decoupled system and both simulations are with the reduced order Luenberger observer. In each case the transfer function gain error within the bandwidth of the compensated beam modes is small however the decoupled model based SPR output design contains a non-minimum phase zero that increases the phase shift by -180 degrees approximately with respect to the minimum phase case. For this reason the coupled model based SPR output was used in all other simulations and experimental tests although it is again emphasized that trial and error was used in the design process, in this case when selecting the synthesized SPR output.

5.3 Experimental Results with Reduced Order Luenberger Observer

Figures 5.9 and 5.10 show the hub angle (a) and first strain gage (b) step responses (experimental) for the two controllers (PD and PD + SPR) with a reference

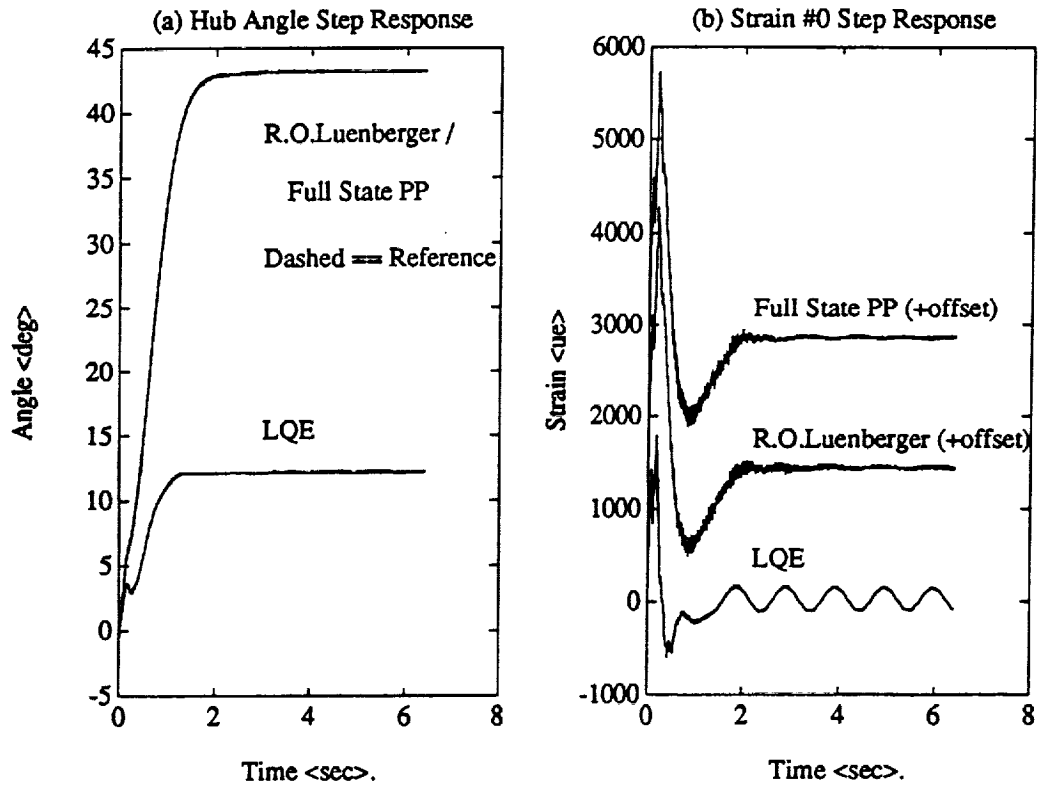


Figure 5.7: Experimental Step Response with Different Observers

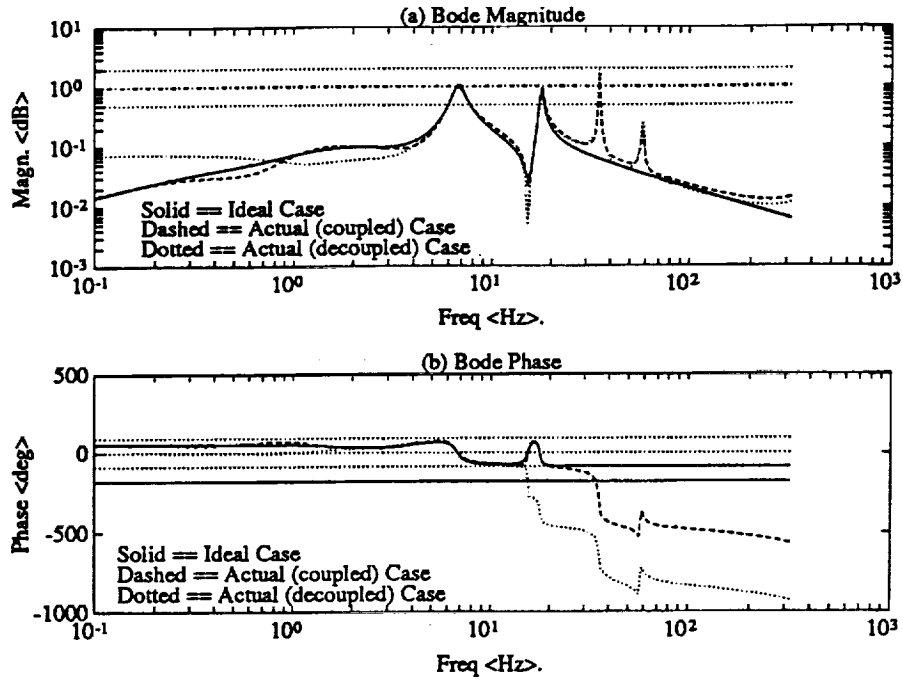


Figure 5.8: Synthesized SPR Output Comparison

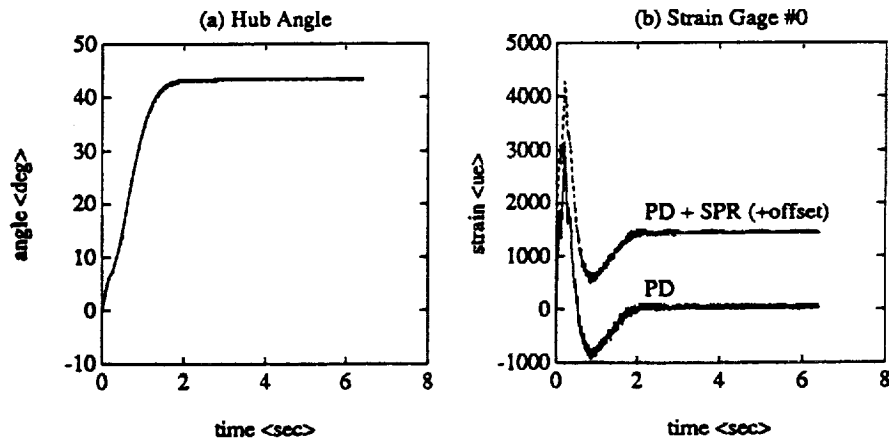


Figure 5.9: Step Response Experimental Results

~~Stabilized~~ PPD + SPR (+offset)

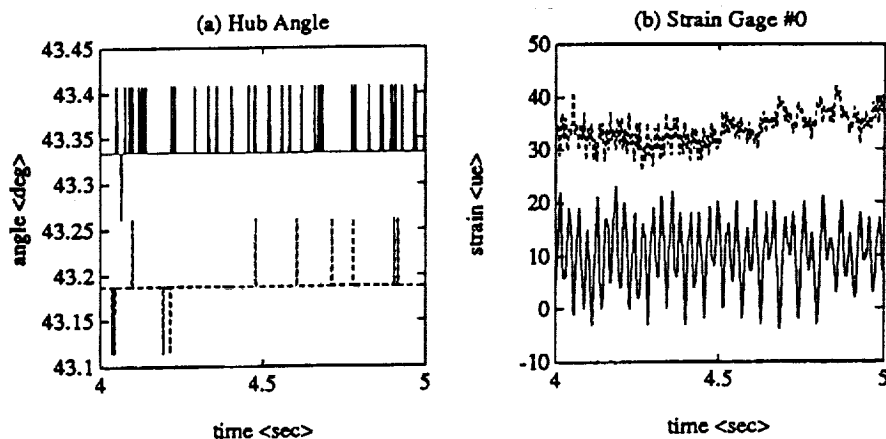


Figure 5.10: Step Response Experimental Results Closeup

step size of 45 degrees. The results are similar to those of the computer simulations which is encouraging however residual oscillations are larger and a steady state error exists due to friction effects at the hub.

As in simulations the PD + S.P.R. controlled system has less residual oscillation than the PD case and an estimate of the increase in damping ratios of closed loop poles for the second and third flexible modes may be obtained by examining magnitude Bode plots derived from experimental results when the beam was excited simultaneously at a range of frequencies, see figure 5.11. In the case of an isolated flexible mode the peak transfer function Bode gain under closed loop differential feedback is inversely proportional to the closed loop pole damping ratio. This effect is distorted with the introduction of other transfer function dynamics, e.g., other flexible modes, however if these modes are sufficiently well spaced apart in the frequency domain and lightly damped than the transfer function close to

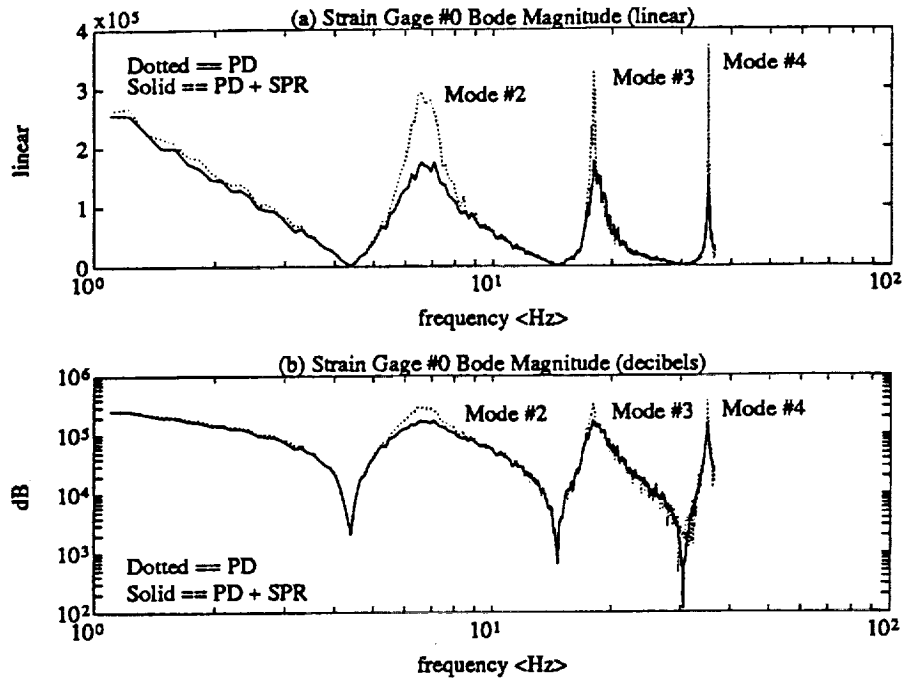


Figure 5.11: Experimental Bode Plots

the center frequency of an individual flexible mode closely approximates that of the corresponding mode and hence in figure 5.11 (a) the reduction in gain magnitudes between the two plots at the flexible mode center frequencies are an approximate indication of the increase in close loop pole damping ratios: an attenuation by a factor of approximately two for the second and third closed loop flexible modes is as predicted by the simulations. Figure 5.11 (b) is a log scale version of figure 5.11 (a) that clearly shows the zeros which are common to the open loop system (see e.g., figure 3.7 part (c)).

CONCLUSIONS

The hub angle PD compensator derived from the linear normal mode model produces very good results in terms of the hub angle step response which has no overshoot and little residual oscillation in both simulations and real tests. The same is also true for the beam tip displacement for the simulated case and although this cannot yet be directly verified for the real testbed case low residual oscillations in the tip displacement are implied by the low residual oscillations in the strain signals.

Adding a second SPR static gain full state feedback loop can improve the step response performance further in a robust manner by increasing the flexible mode pole damping ratios. Such compensation has a phase margin of at least $[-90, 90]$ degrees in the ideal case and this is found to be also true for simulations that include observer effects and some unmodeled modes within the bandwidth of the compensated modes though not at higher frequencies. This suggests the addition of a low pass filter in the SPR feedback loop that maintains a low phase shift and nearly constant gain in the compensated mode bandwidth in order to maintain the low frequency closed loop performance already achieved, with a gain roll off at higher frequencies to attenuate unwanted effects.

Of the three closed loop observers tested the two with poles placed above the highest compensated mode center frequency produced the least distortion on the synthesized SPR transfer function and the best experimental closed loop performance.

The controller design procedure used appears basically sound and produced good results however it is fractured and involved trial and error selections. The task now is to synthesize these observer/compensator blocks either separately or together in a systematic and optimum fashion.

LITERATURE CITED

- [1] Feiyue Wang and John T. Wen. Nonlinear Dynamical Model and Control For A Flexible Beam. CIRSSE Report No.75 Rensselaer Polytechnic Institute, NY, Nov, 1990.
- [2] John.T. Wen. Time Domain and Frequency Domain Conditions for Strict Poistive Realness IEEE Transactions On Automatic Control, Vol. 33, No. 10, October 1988.
- [3] R.H. Cannon, Jr. and E.Schmitz. Precise control of flexible manipulators. In M.Brady and R.Paul, editors, Robotics Research: The First International Symposium, pages 841-861. MIT Press, Cambridge, MA, 1984.
- [4] C. Desoer. Feedback Systems: Input-Output Properties. Academic Press, 1975.
- [5] Chi-Tsong Chen. Linear System Theory and Design. Holt, Rinehart and Winston, Inc., Revised Version, 1984, ISBN 0-03-06-289-0

APPENDIX A

Beam and Actuator Physical Parameters

This appendix contains four tables which list the physical parameters associated with the flexible beam testbed and most are used when deriving the beam model in chapter 3.

Table A.1: Aluminum Beam Material Parameters

Parameter	Symbol	Units	Value
Width	w	m	1.5875e-3
Height	h	m	1.03e-1
Length	l	m	1.098
Density	ρ	Kg/m^3	2.713e3
Youngs Modulus	E	Kg/m^2	6.895e10

Table A.2: Beam Derived Parameters

Parameter	Symbol	Units	Value	Formula
Inertia (about hub axis)	I_b	$Kg.m^2$	1.197e3	$\rho l^3/3$
Cross Sectional Area	A_{bca}	m^2	1.6345e-4	$w.h$
Mass per Unit length	ρ_x	Kg/m	4.4327e-1	$\rho.A_{bca}$
C.S. Area Inertia	I_a	m^4	3.4316e-11	$A_{bca}.w^2/12$
Mass	M_b	Kg	4.436e-1	$w.h.l.\rho$

Note that the actual hub inertia value used in the model is $2.5 \times 10^{-2} Kg.m^2$ (rather than the conservative $2.363 \times 10^{-2} Kg.m^2$ value computed in table A.4) as this was the best approximation at the time. Each mass and inertia was calculated from the dimensions and properties of the system components is only an approximate value that does not take into account fine detail or small objects such as screws etc. Also, the extra mass and inertia due to the light sensor detector and optics currently mounted at the hub are not included in table A.4.

Table A.3: Motor Parameters

Parameter	Symbol	Units	Value
Shaft Inertia	I_m	$Kg.m^2$	1.201e-4
Shaft Mass	M_m	Kg	—
Torque Constant	KT	Nm/A	2.370e-1
Continuous Stall Torque	TS	Nm	1.2407
Peak Torque	TP	Nm	1.358e1
Electrical Time Constant	TE	sec	1.4e-4

Table A.4: Hub Derived Parameters

Item Symbol	Mass M_h Kg	Inertia I_h $Kg.m^2$	#
Motor Shaft		1.201e-4	1
Hub Collar	4.798e-2	3.869 e-6	1
Encoder Collar	—	—	1
Bellows	—	—	1
Potentiometer	—	—	1
Hub Base	1.126	6.707e-3	1
Hub Base Strengthenener	—	—	1
Counter Weight	7.476e-1	1.482e-2	1
Counter Weight Bar	4.123e-2	7.047e-4	1
Balance weight Bar	2.611e-2	3.263e-4	2
Weight Bar Block	3.619e-3	3.000e-5	3
Beam Post	3.941e-1	9.214e-4	2
Hub Assembly total	2.386	2.363e-2	

